# Tridimensional nonhydrostatic transient rip currents in a wave-resolving model

Patrick Marchesiello, Francis Auclair, Laurent Debreu, James C. Mcwilliams, Rafael Almar, Rachid Benshila, Franck Dumas

# Tridimensional nonhydrostatic transient rip currents in a wave-resolving model

Patrick Marchesiello[a,*], Francis Auclair[d], Laurent Debreu[e], James McWilliams[c], Rafael Almar[a], Rachid Benshila[b], Franck Dumas[f]

[a] *IRD/LEGOS, Toulouse, France*
[b] *CNRS/LEGOS, Toulouse, France*
[c] *University of California, Los Angeles, USA*
[d] *LA, University of Toulouse, France*
[e] *Univ. Grenoble Alpes, Inria, CNRS, Grenoble INP, LJK, 38000 Grenoble, France*
[f] *SHOM, Brest, France*

**Abstract**

Flash rips and surfzone eddies are transient horizontal structures of order 10-100 m scale, that can be generated in the surfzone in the absence of bathymetric irregularities. They are traditionally assessed within a depth-averaged framework that involves intrinsic horizontal shear instabilities or/and direct short-crested wave vorticity generation. In this paper, we revisit surf eddy generation processes with a new tridimentional, wave-resolving model (CROCO). We first present a quick overview of a free-surface, compressible approach adapted to nearshore dynamics. Its ability to simulate surface gravity wave propagation and nearshore breaking is validated against laboratory experiments. Next, we present a real-world application of the 3D wave-resolving model to Grand Popo Beach, Benin, forced by waves with frequency and directional spreading. The generation of surfzone eddies by the 3D model is shown to differ considerably from that produced by depth-averaged models, owing to the vertical structure of currents produced by shallow breaking that prevents a strong inverse energy cascade. Processes of both horizontal shear instability and short-crested wave breaking are restricted. Instead, the vertical shear flow is prone to forced variability by wave groups and to a Kelvin-Helmholtz-type instability. The latter shows primary and secondary instabilities, that generate spanwise and streamwise vorticity connecting breaking-induced rolls to larger horizontal surfzone structures. Streamwise filaments, appearing as ribs or mini rips, can extend beyond the surfzone but with lower energy than depth-averaged model rips

(halving offshore mean EKE). Velocity spectra and visual inspection of tracer and sediment concentrations in Grand Popo Beach show much better fit between the 3D model patterns and in-situ and aerial observations. Our results thus propose a plausible demonstration of new 3D nonhydrostatic instability modes and turbulent cascades for the nearshore zone, which will need to be reassessed in a wider range of coastal settings.
*Keywords:* Surfzone, Rip currents, 3D instability, Turbulent cascade, Wave-resolving LES model

## 1. Introduction

Flash rips and surfzone eddies are generally defined as transient horizontal structures of size ranging between water depth and surfzone width, i.e., of order 10-100 m, which are generated in the surfzone in the absence of bathymetric irregularities. They are studied separately from stationary rip currents confined to deeper channels between sandbars (MacMahan et al., 2006; Marchesiello et al., 2015). They are also separated from breaking-induced rollers that scale with wave height (Cox and Anderson, 2001), and even smaller vortices of the fully developed turbulent bore (Svendsen and Madsen, 1984). However, the separation between surf eddies and turbulence is uncertain (Longo et al., 2002) and the possibility of intermediate scales and processes linking horizontal and vertical vorticity generation has been suggested — e.g., Short et al. (1993) describing ephemeral and shallow *mini rips* over Australian low tide terrace beaches — but not clearly demonstrated.

Because it is difficult to sample transient rip currents with sufficient spatial resolution (Lippmann et al., 2016; Henderson et al., 2017), our concepts largely rely on numerical models – depth-averaged, mostly. Three types of processes stand out:

- Horizontal (2DH) shear instability of longshore currents
- Short-crested wave vorticity generation (here called Peregrine process)

*Corresponding author
*Email address:* patrick.marchesiello@ird.fr (Patrick Marchesiello)

- Tridimentional (3D) shear instability

Horizontal shear instability of longshore currents is the earliest process of eddy generation, accounting for the intrinsic variability of wave-driven currents (Bowen and Holman, 1989; Dodd et al., 1992; Allen et al., 1996; Slinn et al., 1998; Özkan-Haller and Kirby, 1999; Dodd et al., 2000; Uchiyama et al., 2009). This process was typically studied with wave-averaged shallow-water models, where momentum transfer from wave to current fields is entirely parametrized. Its importance has faded during the last decade due to prevalence of the Peregrine process, but also to conflicting results given by newly developed wave-averaged tridimentional models (Newberger and Allen, 2007; Splinter and Slinn, 2003).

The second process, largely due to Peregrine (1998), is the current nearshore community views of driving mechanisms for wave-averaged circulation in the surfzone (Kirby and Derakhti, 2019). Boussinesq equations for weakly dispersive intermediate and shallow water waves provides a conceptual model for the action of spatially varying wave breaking, i.e., short-crested waves (Johnson and Pattiaratchi, 2006; Bonneton et al., 2010; Feddersen et al., 2011; Clark et al., 2012; Feddersen, 2014). In this model, small vortices result from generation by differential breaking, and combine over time into larger eddies through an inverse cascade mechanism, consistent with 2D turbulence. The surfzone is thus a production center for eddies with scales roughly ranging from 10 to 100 m. In addition, the coastal boundary imposes that eddies and associated filaments can only go offshore, providing a mechanism for enhanced cross-shore dispersion of various tracers.

The theoretical framework from depth-integrated models neglect the effect of vertical shear. Following the advent of robust 3D formulations of wave-averaged equations (McWilliams et al., 2004; Ardhuin et al., 2008), a number of 3D modeling studies have emerged in the last decade (Newberger and Allen, 2007; Uchiyama et al., 2010; Kumar et al., 2012; Marchesiello et al., 2015; Uchiyama et al., 2017; McWilliams et al., 2018; Akan et al., 2020). They show a modulation of nearshore circulation when wave breaking occurs in a shallow surface layer. However, short-crested wave breaking is generally neglected in these wave-averaged studies (or addressed in ad-hoc manners) and all real-scale applications to

date are performed using hydrostatic assumption, thus underestimating horizontal vorticity motions.

Nonhydrostatic dynamics are essential in our third listed process of surf eddy generation. They are mostly studied in laboratory experiment (Nadaoka et al., 1989) and laboratory-scale Large-Eddy Simulations (LES) using 2.5D CFD models applied to individual wave breaking (Lin and Liu, 1998; Watanabe and Saeki, 1999; Watanabe et al., 2005; Kirby and Derakhti, 2019). These previous studies show that the spanwise (mostly alongshore) component of vorticity is an important aspect of the breaking process. It is associated with vertical shear generated by shallow breaking, which can produce traveling rolls through a primary instability (Watanabe et al., 2005). The rolls, typical of unsteady parallel shear flows, can subsequently evolve through a secondary instability to yield streamwise vorticity, transitioning toward fully tridimensional turbulence. However, 2.5D CFD models are applied to individual breaking waves with only few alongshore wavelengths of the secondary instability, precluding any evaluation of eddy statistics.

3D nonhydrostatic processes are usually studied independently of the two others (by separate research communities) and rarely compared in terms of scales, magnitude and interaction. The only attempt was made by Splinter and Slinn (2003) in a proceeding report. Using a 3D nonhydrostatic model where breaking acceleration is introduced as a body force, they show that deep breaking reproduces 2D model solutions, while the more realistic shallow breaking process seems to disrupt the formation of horizontal shear instability at the expense of vertical shear instability. However, their domain size do not allow statistical comparisons and the profile of breaking acceleration is imposed, not computed from a wave-resolving model. The present study is a step forward from this early work, also addressing the case of short-crested wave generation. Note that (Kumar and Feddersen, 2017) studied transient eddies produced by a 3D nearshore circulation model, forced by short-crested waves computed beforehand with a Boussinesq model. However, wave forcing is prescribed as a depth-uniform body force, i.e., deep breaking, and could not produce vertical shear of the cross-shore flow. Their hydrostatic assumption also precluded the model from vertical shear instabilities.

CROCO (Coastal and Regional Ocean Community model) is a new oceanic modeling system built upon ROMS (Shchepetkin and McWilliams, 2005; Debreu et al., 2012), with added non-Boussinesq kernel (Auclair et al., 2018). CROCO is designed for solving fine-scale processes from the regional ocean to littoral zone with capabilities for LES in realistic configurations. Particular attention is given to numerical accuracy, high-performance computing (optimization, scalability), portability and easy access (`www.croco-ocean.org`). This paper presents a quick overview of the nonhydrostatic CROCO solver with a non-Boussinesq (compressible) approach, before addressing its application to nearshore dynamics. First, its ability to simulate surface gravity wave propagation and nearshore breaking is validated against laboratory experiment. Second, we analyse and validate a full 3D, wave-resolving, real-case simulation of transient rips, in the presence (or not) of short-crested waves and strong alongshore currents. We discuss fundamental differences in the generation of surf eddies by 3D wave-resolving models compared with depth-averaged models, with a focus on the vertical structure of currents produced by shallow breaking and associated turbulence. We conclude on the limitation of simplified vorticity evolution equations in which only the vertical part is considered when so much activity lies in horizontal vorticity, governed by 3D nonhydrostatic equations.

## 2. Model description

Because of limited computational resources, 3D wave-resolving models are still rarely used to study nearshore dynamics in realistic environments. LES applications appeared in the 1990s and are generally restricted to 2.5D laboratory-scale experiments of individual wave breaking. Early applications used the volume-of-fluid (VOF) method for free-surface tracking (e.g., Lin and Liu 1998; Watanabe and Saeki 1999; Watanabe et al. 2005; Derakhti and Kirby 2014). This model type with Cartesian coordinate, where the free surface crosses computational cells arbitrarily, fails to precisely apply the pressure boundary condition on the free surface, affecting the model accuracy.

More recently, several 3D wave-resolving, free-surface and terrain-following models have emerged for the nearshore zone, e.g., SWASH (Zijlema et al., 2011) and NHWAVE (Ma

et al., 2012; Derakhti et al., 2016), based on earlier attempts (e.g., Lin and Li 2002). In this case, explicit free-surface overturning, occurring during breaking, is precluded and must be parametrized as a turbulent or a shock process. However, these models can be accurate as well as computational efficient in the study of waves and wave-driven mean and transient circulation.

CROCO belongs to this class of models but, unlike other attempts, resolves the full compressible Navier-Stokes equations (Auclair et al., 2018). A compressible approach preserves the hyperbolic nature of Navier-Stokes equations and does not require a global elliptic solver with incremental pressure corrections to ensure the incompressible mass balance. As a result, it avoids splitting errors between pressure and velocity and approximations made on free-surface conditions (Zijlema et al., 2011), thereby preserving amplitude and dispersion properties of nonhydrostatic surface waves. In the same time, the absence of global computations by an elliptic solver makes parallelization and optimization procedures much more efficient. The cost of solving acoustic waves is managed with a time-splitting technique and semi-implicit time discretization, introduced below.

The development of CROCO around the Regional Oceanic Modeling System (ROMS) has advantages for realistic LES applications. It benefits from capabilities long developed in oceanic models – high-performance computing; high-order discretization; coupling with biogeochemistry and sediment models; pre-processing tools for fast model input generation. The nonhydrostatic model version can thus be applied without much effort to realistic, highly nonlinear regimes, e.g., large internal solitons and hydraulic jumps (Hilt et al., 2020), Kelvin-Helmholtz instabilities (Penney et al., 2020), or wave-induced nearshore circulation as in the present study. It is naturally suited for bridging ocean and coastal sciences, e.g., addressing surf-shelf exchange processes in a 3D, rotating and stratified framework. In addition, both wave-resolving and wave-averaged (Uchiyama et al., 2010; Marchesiello et al., 2015) model equations are available within the same code, which has potential benefits for evaluating parametrizations of wave-current interactions in wave-averaged models.

*2.1. Free-surface, compressible ocean model equations*

The full set of Navier-Stokes equations for a free-surface ocean is explicitly integrated in the nonhydrostatic, non-Boussinesq (compressible) version of CROCO, built upon the code structure of ROMS primitive equation solver. In the compressible approach (Auclair et al., 2018), acoustic waves are solved explicitly to avoid Boussinesq degeneracy, which inevitably leads to a 3D Poisson system in nonhydrostatic incompressible methods – detrimental to computational costs and accuracy of free-surface model implementation.

Non-Boussinesq equations include the momentum and continuity equations, the surface kinematic relation (for free surface), heat, salt or other tracer $C$ conservation equations, and the equation of state, which reads in Cartesian coordinates:

$$\frac{\partial \rho u}{\partial t} = -\vec{\nabla}.(\rho \vec{\mathbf{v}} u) + \rho f v - \rho \tilde{f} w - \frac{\partial P}{\partial x} + \mathcal{F}_u + \mathcal{D}_u + \lambda \frac{\partial \vec{\nabla}.\vec{\mathbf{v}}}{\partial x} \tag{1}$$

$$\frac{\partial \rho v}{\partial t} = -\vec{\nabla}.(\rho \vec{\mathbf{v}} v) - \rho f u - \frac{\partial P}{\partial y} + \mathcal{F}_v + \mathcal{D}_v + \lambda \frac{\partial \vec{\nabla}.\vec{\mathbf{v}}}{\partial y} \tag{2}$$

$$\frac{\partial \rho w}{\partial t} = -\vec{\nabla}.(\rho \vec{\mathbf{v}} w) + \rho \tilde{f} u - \frac{\partial P}{\partial z} - \rho g + \mathcal{F}_w + \mathcal{D}_w + \lambda \frac{\partial (\vec{\nabla}.\vec{\mathbf{v}})}{\partial z} \tag{3}$$

$$\frac{\partial \rho}{\partial t} = -\vec{\nabla}.(\rho \vec{\mathbf{v}}) \tag{4}$$

$$\frac{\partial \eta}{\partial t} = \ w_f|_{z=\eta} - \vec{\mathbf{v}}|_{z=\eta}.\vec{\nabla}\eta \tag{5}$$

$$\frac{\partial \rho C}{\partial t} = -\vec{\nabla}.(\rho \vec{\mathbf{v}} C) + \mathcal{F}_C + \mathcal{D}_C \tag{6}$$

$(u, v, w)$ are the (x,y,z) components of vector velocity $\vec{\mathbf{v}}$; $\eta$ is the free surface; $\phi(x, y, z, t)$ is dynamic pressure $\phi = P/\rho_0$, with $P$ the total pressure; $\rho_0 + \rho(x, y, z, t)$ is total *in situ* density; $f(x, y)$ and $\tilde{f}(x, y)$ are the traditional and non-traditional Coriolis parameters, function of latitude; $g$ is acceleration of gravity; $\mathcal{D}_u, \mathcal{D}_v, \mathcal{D}_C$ are diffusive terms; $\mathcal{F}_u, \mathcal{F}_v, \mathcal{F}_C$ are forcing terms; $\lambda$ is the second (bulk) viscosity, associated with compressibility (used to damp acoustic waves).

*2.2. Time-splitting principle*

In the above set of equations, a relation between $\rho$ and $P$ is required. To that end, and as part of a time-splitting approach, density is decomposed into slow and fast components based on a first-order linear decomposition with respect to total pressure. In the following, $s$ and $f$ subscripts refer to slow and fast-mode components respectively:

$$\rho = \rho_s(T, S, P_s) + \overbrace{\left.\frac{\partial \rho}{\partial P}\right|_{T,S} \delta P}^{\rho_f = c_s^{-2} P_f} + O(\delta P^2) \tag{7}$$

$$P = \underbrace{P_{atm} + \int_z^\eta (\rho_s - \rho_0) g \; dz'}_{SLOW} + \underbrace{\rho_0 g(\eta - z) + \overbrace{\delta P}^{P_f}}_{FAST} \tag{8}$$

$c_s$ is the speed of sound and $\delta P = P_f$ is the nonhydrostatic pressure.

The Navier-Stokes equations are then integrated with two different time steps within the time-splitting approach inherited from ROMS. The slow-mode integration is similar to ROMS with the addition of the slow part of vertical momentum equation, whereas fast-mode integration is 3D and includes the compressible terms of momentum and continuity equations. In vector form:

$$\begin{aligned} \frac{\partial \rho \vec{\mathbf{v}}}{\partial t} = & \underbrace{-\vec{\nabla}.(\rho \vec{\mathbf{v}} \otimes \vec{\mathbf{v}}) - 2\rho \vec{\Omega} \times \vec{\mathbf{v}} - \vec{\nabla}(\int_z^{\eta_f} (\rho_s - \rho_0) g \; dz') + \vec{\mathcal{F}}_{\vec{\mathbf{v}}} + \vec{\mathcal{D}}_{\vec{\mathbf{v}}}}_{SLOW} \\ & \underbrace{-\rho_0 g \vec{\nabla} \eta_f - \vec{\nabla} P_f + \rho_f \vec{\mathbf{g}} + \lambda \vec{\nabla}(\vec{\nabla}.\vec{\mathbf{v}})}_{FAST} \end{aligned} \tag{9}$$

$$\frac{\partial \rho_f}{\partial t} = -\frac{\partial \rho_s}{\partial t} - \vec{\nabla}.(\rho \vec{\mathbf{v}}) \tag{10}$$

$$P_f = c_s^2 \; \rho_f \tag{11}$$

$$\frac{\partial \eta_f}{\partial t} = \; w_f|_{z=\eta} - \vec{\mathbf{v}}_f|_{z=\eta}.\vec{\nabla} \eta_f \tag{12}$$

$$\frac{\partial \rho C_s}{\partial t} = -\vec{\nabla}.(\rho \vec{\mathbf{v}} C_s) + \mathcal{F}_C + \mathcal{D}_C \tag{13}$$

$$\rho_s = \rho(T_s, S_s, \eta_f) \tag{14}$$

$$\rho = \rho_s + \rho_f \tag{15}$$

The momentum is integrated both in slow and fast modes but the right-hand-side of the equation is split in two parts: a slow part, made of slowly varying terms (advection, Coriolis force, baroclinic pressure force and viscous dissipation), and a fast part, made of fast-varying terms (the surface-induced and compressible pressure force, weight, and dissipation associated with bulk-viscosity). This momentum equation is numerically integrated twice, once with a large time-step keeping the fast part constant, and once with a smaller time-step keeping the slow part constant. This is much more computationally efficient than integrating the whole set of equations at the same fast time step. More details can be found in Auclair et al. (2018)[1].

Note that acoustic waves can become pseudo-acoustic if their phase speed $c_s$ is artificially reduced ($c_s$ is a model parameter). In this case, high-frequency processes associated with bulk compressibility may be unphysical, but an accurate solution for slower nonhydrostatic dynamics can be preserved, while relaxing CFL constraints.

### *2.3. Discretized equations for nearshore application*

In this study, motions are produced by an offshore wave-maker in a non-rotating, homogeneous fluid. In this case, the Coriolis force, baroclinic pressure force and all surface fluxes are null. There is no temperature or salinity stratification so that slow density $\rho_s$ is constant in time and space.

[1]Auclair et al. (2018) presents a first implementation of the compressible approach involving a 3-level time splitting (internal, external and acoustic). CROCO was simplified to only retain a slow and a fast time level, where acoustic waves are solved together with the external (depth-averaged) mode. This procedure is more computationally efficient

CROCO is discretized on a C-grid with finite-difference methods for slow and fast modes that are detailed elsewhere (Shchepetkin and McWilliams, 2005; Soufflet et al., 2016). In short, the slow-mode time-stepping algorithm is a Leapfrog Adams-Moulton predictor-corrector scheme, that is third-order accurate for the integration of advective terms. The fast mode is integrated with a generalized forward-backward scheme, which is also third-order accurate. Vertical flux terms that do not require accuracy (vertical diffusion term in the slow mode and all acoustic terms of $w$ equation in the fast mode) are computed with an implicit time stepping to increase computational stability.

Horizontal and vertical advection terms are discretized using the WENO5-Z improved version of the 5th-order weighted essentially non-oscillatory scheme (Borges et al., 2008), which is popular for hyperbolic problems containing both shocks and smooth structures. WENO5-Z naturally copes with dispersive numerical modes as well as shocks caused by breaking waves, with no need for ad hoc criteria. Additionally, a 3D Smagorinsky model is used for turbulent closure on anisotropic grids:

$$\nu_t = (C_S \Delta)^2 \, |S| \tag{16}$$

where the 3D strain rate $|S| = \sqrt{2 S_{ij} S_{ij}}$, with $S_{ij} = \frac{1}{2}(\frac{\partial u_i}{\partial x_j} + \frac{\partial u_j}{\partial x_i})$ (using Einstein notation); $\Delta$ the grid-characteristic length scale, i.e. the grid size: $\sqrt{\delta_x \delta_y}$ for horizontal viscosity and $\delta_z$ for vertical viscosity, where $(\delta_x, \delta_y, \delta_z)$ are mesh sizes in (x,y,z) directions. $C_S$ is the Smagorinsky coefficient, taking a standard value of 0.1 (Canuto and Cheng, 1997; Christensen and Deigaard, 2001), although the sensitivity of model results to this value is discussed along the paper. Alternatively for some tests, a $k - \epsilon$ model, solving closure equations for turbulent kinetic energy $k$ and dissipation $\epsilon$, was used as part of a Generic Length Scale (GLS) method (Warner et al., 2005). In this case, turbulent viscosity $\nu_t = c_\mu \, l \, k^{\frac{1}{2}}$, with coefficient $c_\mu$ dependent on stability functions, and mixing length scale $l \propto k^{\frac{3}{2}} \epsilon^{-1}$. Here, $l$ is independent of resolution, which is more strictly associated with RANS (Reynolds-Averaged Navier-Stokes equations) than LES. All $k - \epsilon$ model parameters are standard (Warner et al., 2005).

### 2.4. Wave maker at offshore boundary

The wave maker forces a spectrum of 3D linear waves at the offshore boundary, as in Zijlema et al. (2011), rather than as an interior source term (Wei et al., 1999). The spectrum has frequency and directional spreading similar to Feddersen et al. (2011):

$$\eta_{bc}(y,t) = \sum_i a_i \sum_j d_j cos(k_{y,ij} y - \omega_i t - \phi_{ij}) \tag{17}$$

$$\text{with } d_j = \mathrm{e}^{-\frac{\theta_j - \theta_m}{\sigma_\theta^2}} \text{ and } \sum d_j = 1 \tag{18}$$

$$u_{bc}(y,t) = \eta_{bc}(y,t)\ \omega_p\ cos(\theta_m)\ \frac{cosh(k_p(z+h))}{sinh(k_p h)} \tag{19}$$

$$v_{bc}(y,t) = \eta_{bc}(y,t)\ \omega_p\ sin(\theta_m)\ \frac{cosh(k_p(z+h))}{sinh(k_p h)} \tag{20}$$

where (x,y,z) are cross-shore, alongshore and vertical directions respectively; $(i,j)$ are indices of spectral distribution in frequency and direction respectively; $a_i$ is the amplitude at each frequency $\omega_i$, from a given statistical distribution, e.g., JONSWAP (Sec. 4.1); $k_{y,ij} = k_i\ sin(\theta_j)$ is the alongshore wavenumber, where $k_i$ is the linear theory wavenumber: $\omega_i^2 = g\ k_i\ tanh(k_i h)$, and $\theta_j$ is wave angle; $\theta_m$ is the mean wave direction and $\sigma_\theta$ the directional spread around the mean; $\omega_p$ and $k_p$ are peak frequency and wavenumber; $d_j$ is a normalized frequency-dependent directional distribution; $\phi_{ij}$ is a uniformly distributed random phase.

Here $w_{bc}$ is set to zero and our tests show only weak sensitivity to this choice. Depth-averaged (barotropic) velocities $(\bar{u}, \bar{v})$ must be provided as well in the wave maker because they are prognostic variables of our split-explicit model, advanced together with the fast acoustic mode. Normal depth-averaged velocity $\bar{u}$ is complemented at the boundary by a "compensation flow", opposite to Stokes drift and thus closing the volume budget. We do not impose the depth-averaged value of $u_{bc}$ directly but the value of the incoming characteristic of the shallow water system as in Flather-type conditions (Marchesiello et al., 2001; Blayo

and Debreu, 2005):

$$\bar{u} = \bar{u}_{bc} - \sqrt{\frac{g}{h}}(\eta - \eta_{bc}) \tag{21}$$

This allows infragravity waves generated inside the domain to propagate out as long waves, while ensuring a near conservation of mass and energy through the open boundary. Similarly, the baroclinic components ($u_{bc}$,$v_{bc}$,$w_{bc}$) are applied through an adaptive radiation condition that allows 3D flow perturbations to leave the domain without deteriorating the interior solution (Marchesiello et al., 2001).

## 3. Validation in Flume experiment

### *3.1. GLOBEX experiment*

As a first step towards 3D modeling, we present here a validation of wave propagation and breaking using a wave flume experiment. The Gently sLOping Beach EXperiments (GLOBEX[2]) were performed in the Scheldt flume of Deltares (Delft, the Netherlands) in 2012, and described in Michallet et al. (2014). The project objective was to collect high-resolution space-time data of the cross-shore evolution of short and infragravity waves on a gentle slope for a range of wave conditions.

The flume is 110 m long, 1 m wide and 1.2 m high. The waves were generated with a piston-type wave maker equipped with Active Reflection Compensation to minimize reflections from the wave paddle. A concrete beach with a weakly reflexive 1:80 slope was constructed, with its toe at 16.57 m from the wave maker. All experiments were run with a still water depth of 0.85 m and still-water shoreline at $x = 84.57$ m. The material that was laying loose on the concrete bed before the flume was filled with water had a median grain size D50=0.75 mm (roughness length $z_0 \sim D50/12 = 0.0625$ mm).

Sea-surface elevation measurements were taken at 190 locations (repeating an experiment ten times while relocating the 21 wave gauges), together with velocity measurements at 43 locations, mostly (but not always) at 1 cm above bed to focus on the undertow. The sampling frequency of the instruments during these experiments is 128 Hz. Here, we focus

[2]Globex data is freely available at `zenodo.org/record/4009405`

on one of the experiments, B3, corresponding to second-order (Stokes) wave generation of bichromatic frequencies (simulated with a Boussinesq model in Michallet et al. 2014). The characteristics are as follows: $a_1 = 0.09$ m; $a_2 = 0.01$ m; $f_1 = 0.420$ Hz; $f_2 = 0.462$ Hz (short-wave peak period $T_p = 2/(f_1 + f_2) = 2.27$ s; and group period $T_g = 1/(f_2 - f_1) = 23.81$ s). The signal had a total duration of 75 minutes.

### *3.2. Model comparison*

The model is set-up with the same conditions as the wave flume experiment. Second-order bichromatic waves are generated at the offshore boundary, with shore normal direction and zero directional spread. A no-slip condition is imposed on the lateral wall boundaries of the canal so that transverse modes are precluded.

Figure 1 compares an Hovmuller plot (x,time) of data and model sea level $\eta$ and undertow $u_b$. $u_b$ is interpolated at the measurement depth assuming a logarithmic profile. When data is missing in the measurements, it is also removed from the model output. The general structure reflecting wave speed and frequencies, wave packets, surf and swash zones are all very similar. Model-data correlations are high with 0.85 and 0.77 respectively for $\eta$ and $u_b$, and root mean square errors are 2 cm and 0.13 m/s. Some scattering in the undertow data is noticeable. According to Michallet et al. (2014), it may be attributed to the presence of secondary motions generated by transverse waves at the break point where the transverse mode-1 seiche can be excited at frequency $f_1 + f_2$. It may also be due to variations in depth level of flow measurements in the surf zone.

A snapshot of wave field across the flume during runup condition is presented in Figure 2. It highlights the main processes of propagation, nonlinear interaction, shoaling, breaking, roller propagation and runup. Model-data correlation is high, as already mentioned, and non-linearity is apparent in both cases in the increasingly non-sinusoidal shape of short waves as they approach the shore (Elgar and Guza, 1985). They first develop short, high wave crests with increasing skewness (asymmetry about the horizontal axis, measuring crest/trough shape), and as they break, transition into the characteristic saw-tooth shape with asymmetry about the vertical axis.

Wave statistics (first, second and third moments) for $\eta$ and $u_b$ are shown in Figure 3: mean, standard deviation (or $H_s$ for $\eta$), skewness $\langle \phi'^3 \rangle / \langle \phi'^2 \rangle^{1.5}$ and asymmetry $\langle \mathcal{H}(\phi')^3 \rangle / \langle \phi'^2 \rangle^{1.5}$ ($\mathcal{H}$ is Hilbert transform). For the mean field of measured undertow, a few scattered points lying far outside the standard deviation are removed using a polynomial fit. With this, the model appears to replicate the observed cross-shore undertow profile (top-left of Fig. 3). The undertow is part of a vertical recirculation associated with breaking-induced surface onshore flow. It may be considered a proxy of the vertical shear, which will appear as an essential parameter of surfzone eddy generation in the next section. Here, we call undertow the bottom return flow (10 cm/s in this experiment). There is also an Eulerian compensation flow for the onshore surface Stokes drift (continuity of total flow must be preserved), which is sometimes referred to as undertow. This compensation flow is the only cross-shore flow captured by depth-averaged models and is relatively weak (on the order of 1 cm/s in this simulation). In Figure 3, the model also properly represents the envelop of high-order moments. Details of skewness and asymmetry may differ in model and data, due in part to irregular current measurement depth and transverse modes in surfzone measurement, but the evolution and transition from high skewness to high asymmetry is similar. Apart from somewhat higher skewness and lower asymmetry than measured in the breaker zone, we conclude that nonlinear shoaling, breaking-induced wave transformations and – maybe more importantly for the present study – the surfzone recirculation are generally well reproduced.

From sensitivity tests, it appears that a realistic reproduction of $H_s$ cross-shore evolution in the breaker zone ($x = 60 - 70$ m) is conditioned to using the shock capturing scheme WENO5-Z. The results are degraded (not shown) when replacing WENO5-Z with UP5, a non-monotonic linear upstream-biased 5th-order advection scheme (Menesguen et al., 2018). The Smagorinsky model alone (or alternatively a $k-\epsilon$ model) was less efficient in dissipating the breaking wave front. This is in line with analogies between breaking waves, bores and hydraulic jumps, that may be treated as a shock (Cienfuegos et al., 2010; Tissier et al., 2012; Lubin and Chanson, 2017). On the other end, the WENO scheme is less efficient in the roller zone ($x > 70$ m), where turbulent dissipation dominates over production (van der A et al., 2017). There, the turbulent closure scheme takes over as main dissipation process.

Therefore, our combination of numerical and physical closure with off-the-box parameters provides a realistic framework for surfzone dynamics. The fact that no tuning was needed for these schemes and that there is no ad hoc detection and treatment of wave breaking provides confidence in applying the model to other configurations.

## 4. Natural beach application

We now turn to a full 3D experiment with longshore-uniform bathymetry. The configuration is derived from Grand Popo Beach (6.2°N, 1.7°E, Benin, in the Gulf of Guinea; Fig. 4). This stretch of coast presents a longshore-uniform, low tide terrace and steep upper shoreface (Almar et al., 2014, 2016) and a sandy wave-dominated and microtidal environment, exposed to S-SW long period swells generated at high latitudes in the South Atlantic (Almar et al., 2015a). A field experiment was conducted at Grand Popo Beach from 10 to 18 March 2014 (Almar et al., 2014; Derian and Almar, 2017). For our setup, we focus on conditions in the middle of the afternoon of March 13 2014. The weather, tides and wave conditions were ideal: weak winds and wind waves well separated from a narrow-band swell with significant wave height $H_s = 1.15$ m, peak period $Tp = 11$ s, and wave incidence $D = 10°$ from shore normal direction (measured from an Acoustic Doppler Current Profiler moored in 10-m depth). The water was at mid neap tide level (low-tide terrace at about 1 m depth), promoting a narrow surfzone less than 50 m wide. A Nortek high-frequency acoustic Doppler velocimeter (ADV with sampling rate of 8 Hz) was deployed in the surfzone, in the middle of the terrace, measuring currents about 0.5 m from the bottom. A dye release was conducted to monitor the dispersion induced by flash rips, coupled with UAV flights (STB DS6 hexacopter) at an elevation of 100 m. The Drone camera (NIKON D700) was looking down, with a vertical angle, and recorded 4256×2832-px scenes at 1 Hz (Almar et al., 2014; Derian and Almar, 2017).

### *4.1. Model Setup*

The domain is 542 m alongshore by 240 m across-shore, with periodic alongshore boundary conditions. In order to prevent distortion when oblique waves are used with periodic

conditions, the alongshore size is adjusted according to peak wavelength and mean wave direction. This method proved to perform well even with long-crested waves. The grid spacing is generally $dx = dy = 1$ m but one simulation is run with higher resolution of 0.5 m. There are 10 vertical levels evenly spaced between the free surface and bottom (a simulation with 20 levels did not change the results much). The model time step is $dt = 0.025$ s (0.0125 s at 0.5 m resolution). The model bathymetry is longshore-uniform and built with continuous functions to smoothly fit the low-tide terrace structure observed during the survey of (Almar et al., 2014, 2018). Depth $H$ is 8 m offshore to 1 cm at the shoreline, whose position varies with swash oscillation, relying on a wetting-drying scheme (Warner et al., 2013). Depth over the terrace is about 1 m according to the afternoon mid-tide conditions of March 13 2014.

The wave maker is set with following parameters: $H_s$=1.15 m, $Tp$=11 s, $D = 0°$, $10°$ or $20°$ ($D = 10°$ for comparison with data in Sec 4.3), and directional spread $\sigma_\theta = 30°$. A JONSWAP spectrum is constructed with these parameters and a peak enhancement factor $\gamma$ of 3.3. The quasi-monotonic and shock-capturing WENO5-Z scheme is used again with Smagorinsky turbulence closure and $C_S = 0.1$. Bottom roughness is $z_0 = 0.01$ mm, which may seem low but gives a drag coefficient $C_D \sim 0.002$ in the surfzone ($C_D = \kappa^2/ln(z_1/z_0)^2$, with $\kappa = 0.41$ and $z_1 \sim H/10$ the first level height above bed), which is a usual value in depth-averaged models (Chen et al., 2003; Feddersen et al., 2011). We follow the practice of these models here to reproduce their results within the pseudo-2D approach described below. It is of little consequence for 3D simulations because, as will be shown, they are much less sensitive to bottom drag than 2D models (Sec. 5).

The model is run for an hour starting from rest and adjusting through a rapid spin-up phase. Figure 5 shows a snapshot of sea level that shows realistic features: short-crested waves generated at an angle refract and break, generating rollers, swash and some reflection.

CROCO comes with capabilities for water quality, marine ecosystem and sediment modeling. In the present study, some of these capabilities are used with simple settings. First, we introduce a passive tracer in the swash zone for comparison with dye releases made during the beach survey. Second, a suspended sediment model (Blaas et al., 2007; Warner et al., 2008) allows comparison of rip patterns with aerial photos taken during the survey. We

use a single fine sand class with settling velocity of 1 cm/s. For resuspension, taking one sediment bed layer for simplicity, only two parameters are needed: critical shear stress and erosion rate at the seafloor, expressed in the erosion flux (Blaas et al., 2007):

$$E = E_0(1-p)\left(\frac{\tau_b}{\tau_{cr}} - 1\right) \quad \text{for } \tau_b > \tau_{cr}$$

$$E = 0 \quad \text{otherwise}$$

$\tau_b$ is the bottom shear stress computed by the model. $E_0$ is an empirical erosion rate set to $10^{-5}$ kg/m$^2$/s; $p$ is the sediment porosity (0.41); $\tau_{cr}$ is the critical shear stress, i.e., the threshold for initiation of sediment motion, set to 0.01 N/m$^2$.

### *4.2. Shallow vs. deep breaking (and a Boussinesq model)*

The Peregrine vorticity generation process only requires short crested waves, with no need for unstable longshore currents generated by oblique waves. Boussinesq models are very efficient in this process, but an important question for us is whether a 3D model will remain so. An essential difference between the two types of model is the depth penetration of wave breaking. In a 2D Boussinesq model, deep breaking is implicitly assumed as momentum is transferred instantaneously to the depth-averaged flow. However, this is a crude assumption as breaking-induced flow and turbulence is produced essentially above trough level (where the onshore flow is located), while turbulence at deeper levels depends more on vertical diffusion and less on local production (Grasso et al., 2012; van der A et al., 2017). (Uchiyama et al., 2010) show that the deep breaking assumption is inconsistent with high-resolution cross-shore velocity profiles measured during Duck94. Splinter and Slinn (2003) also suggest that transient dynamics produced by deep breaking may collapse in the more realistic case of shallow breaking. The results presented here are in agreement with these studies and we propose to assess the role of 3D dynamics on surf eddies by comparing simulations forced by shallow and deep breaking. Deep breaking will constitute a pseudo-2D model whose results can be compared with a Boussinesq model solution (Section 4.5).

Boussinesq-type models (see Barthelemy 2004, for a review) are common tools to simulate weakly dispersive waves and their transformations from the ocean to the swash zone. Several

developments allowed their application to a wide range of scales, from surfzone processes to ocean basin–scale tsunami propagation (Kirby, 2016). Here, for a verification of our pseudo-2D CROCO version, we use FUNWAVE-TVD (Shi et al., 2012). It solves the fully nonlinear Boussinesq equations using a hybrid finite-volume finite-difference scheme. Parametrizations are similar to CROCO, with wave breaking handled by a shock capturing TVD scheme (making the need of explicit criterion unnecessary) and a quadratic drag formulation with $Cd = 0.002$ for bottom friction. Note that newer generation models than FUNWAVE are available with better dispersive properties — using Green-Naghdi equations (Lannes and Bonneton, 2009) or incorporating an additional enstrophy equation (Kazakova and Richard, 2019) — but FUNWAVE is widely used and share with this class of models the essential depth-averaged assumption.

To force deep breaking in a 3D wave-resolving model, we can artificially enforce strong, deep vertical mixing around the breaker zone by multiplying the vertical turbulent viscosity by 500 ($\nu_t \sim 1\ m^2/s$, on the vertical only). Figure 6 shows a time and longshore average of cross-shore and alongshore currents in the case of shallow and deep breaking. Shallow breaking is computed by the 3D model with no explicit constrain on penetration scale (but a parametrization of turbulence induced by breakers and currents). It drives a shallow onshore flow about 40 cm deep and an offshore near-bottom undertow, resulting in strong vertical shear of about 2 m/s within 1 m depth. With artificially strong vertical viscosity, momentum in the breaker zone is almost instantly mixed to the bottom and the cross-shore flow is reduced to nearly zero as required by mass-conservation (the residual flow is the Stokes drift compensation flow), and consistent with depth-averaged models. The longshore flow driven by oblique waves and a number of other simulations with shallow and deep breaking (Tab. 2) will be analyzed and compared in the following sections.

### *4.3. Reference simulations and comparison with data*

To introduce the 3D processes of flash rip generation, we present simulations with shallow and deep breaking (3D_SC_D10 and 2D_SC_D10), representing mid-tides conditions on March 13 2014 in Grand Popo Beach. Figure 7 compares the vertical vorticity of surface

flow: $\omega_z = \frac{\partial v_s}{\partial x} - \frac{\partial u_s}{\partial y}$, averaged over two peak periods (22 s). With deep breaking (left panel), the vortical field is rich with large filaments and surf eddies of 50-100 m scale that are generated from short-crested waves, similar to Boussinesq model solutions. However, the full 3D model with shallow breaking offers a radically new solution (Fig. 7, right panel). Some of the large-scale fluctuations are present but over-shadowed by shorter scales. This mode presents itself as rib structures (or mini rips following a relevant observation by Short et al. 1993, already mentioned) with short longshore wavelength of order 5-10 m and periods less than 5 min.

We now compare the two simulations with data collected during the survey of March 2014. Flash rips did not strike the survey team as particularly imposing (Castelle et al., 2014; Scott et al., 2018; Floc'h et al., 2018). Dye experiments revealed filament generation, but of relatively short scales. The survey was not extensive in terms of spatial resolution but ADV and dye observations suggested a dynamical regime much closer to 3D shallow-breaking than pseudo-2D deep-breaking simulations, as will be seen.

The dye experiment presented in Figure 8 illustrates both the structure of the alongshore flow and scales of flash rips emerging from the surfzone. Careful analysis of observed versus modeled dye evolution, as in Hally-Rosendahl and Feddersen (2016), is beyond the scope of this paper, but useful information can be gained from a simpler analysis. Figure 8 presents two consecutive aerial photos (at 154 s interval), and the corresponding snapshots of tracer simulations with the full 3D model. We do not expect an exact match between observed and modeled rips, considering the chaotic nature of these phenomena, but scales and structures are meaningful. During the survey, a few attempts of dye release were made before obtaining a clear filament patch. Similarly for the model, we selected one occurrence among few tracer patches initialized at regular interval along the coast (in the swash zone). Even though all tracer patches eventually ended up with similar V-shape and similar scales of evolution, there was variability in the evolution and we selected the most visually comparable filament with Drone photos. In both cases, a thin filament of 5-10 m expands quickly seaward at a speed of about 0.5-1 m/s, reaching about 70 m from shore. Using sequential photos of the tracer from the Drone camera, it is also possible to extract a simplified cross-shore profile of longshore

drift velocities (see Derian and Almar 2017 for more extensive Lagrangian calculations). The result is presented in Figure 9 together with the ADV measurement of mean longshore current over the terrace and model solutions with deep and shallow breaking. The estimated longshore flow has an asymmetric V-shape very similar to the full 3D model solution with a peak velocity of about 0.4 m/s in the inner surfzone, and error bar of about 0.1 m/s (Derian and Almar, 2017). Deep breaking solutions have a more symmetric profile centered in the outer surfzone. The profiles in both simulations are a result of cross-shore advection. With deep breaking, advection is weak and the longshore flow remains centered in the breaker zone (Fig. 6). This is also a common bias of depth-averaged models (Larson et al., 2002).

Another qualitative comparison of patterns can be made, looking at surfzone suspended sediments in the aerial photo (Fig. 10, left panel). The contrasts in the photo is enhanced to better expose suspended sediments (brown color), which is seen weakly extending beyond the surfzone. Snapshots of the model's surface sediment concentration is also shown after 15 min of simulation. With shallow breaking (center panel), sediments tend to resuspend in the breaker zone and mix efficiently within the surf zone, but only weakly extend to the innershelf. The rib structure is apparent at the seaward front of sediment concentration. It is also apparent in alongshore convergence lines that have a structure similar to the foam lines in the aerial photo. Overall, the patterns are very similar to the observations, particularly in the upper part of the photo, where there is less foam or sunglint. The same suspended sediment simulation with deep breaking gives very different results (Fig. 10, right panel). Resuspension is now maximum in the inner surfzone (as for eddy energy; Sec. 4.5). Filaments and eddies are more coherent, larger, their growth slower, but they extend much further seaward. Mixing in the surfzone is less efficient than for the shallow-breaking case, but shelf-surf exchange is more intense, due to filament extension. This more coherent pattern may have aesthetic values but does not fit visual observations of Grand Popo Beach.

For a more quantitative local comparison, we used ADV measurements, looking at horizontal $u_h = \sqrt{u^2 + v^2}$ and vertical $w$ velocities, the latter being a good indicator of 3D motions. Figure 11 presents Power Spectral Density (PSD), using Welch's method of noise reduction, of $u_h$ and $w$ velocity fluctuations for the model and the ADV data at a similar

location in the middle of the terrace. The short-wave spectrum around the peak period (11 s) is well represented considering that the model wave maker uses a JONSWAP approximation. At lower frequency in both $u_h$ and $w$ PSD, a good fit with data is given by the full 3D model, while the deep-breaking simulation has a clear energy deficit (valid at 95% confidence level). Looking at $u_h$ PSD, there is a band of high energy around 30-100s period that is clearly missing in the pseudo-2D case. This frequency is consistent with visual inspection of rip structure oscillation in animated vorticity fields. However, the difference between 3D and pseuso-2D cases can be seen at even lower frequency. This is best illustrated by $w$ PSD and will be shown to result from nonlinear upscaling (Sec. 4.6). Interestingly, the energy range of 3D eddies encroaches on that of infragravity waves, making it hard to separate the two dynamics from observations alone.

On the innershelf, about 80 m offshore where unfortunately no data is available, the comparison between model simulations shows a different relation at very low frequency, for time scales between 3 and 15 min (Fig. 12). In this range, eddies produced by short-crested waves have more energy in the deep-breaking case, as expected from visual inspection of vorticity and suspended sediments. We conclude from this section that observations in Grand Popo Beach are in better agreement with a full 3D solution of surf eddies, which presents a radically different dynamical regime. We will now analyze more closely the 3D structure and generation process of rib structures.

### *4.4. Structure and production of vertical shear instability*

The surfzone eddy variability seen in the 3D model solution is truly three-dimensional. Vertical vorticity is only one manifestation, but horizontal vorticity is the key player. For better detection, we use a higher-resolution simulation ($dx = dy = 0.5$ m; run for 15 minutes) that gives a very similar solution to the lower resolution case. Figure 13 presents the Q field defined by $Q = -\frac{1}{2}\frac{\partial u_i}{\partial x_j}\frac{\partial u_j}{\partial x_i}$, using Einstein summation convention over the three dimensions. Q is commonly used to enhance detection of vortical flows. Here, we split cross-shore and alongshore Q components ($Q_y = -\frac{\partial u}{\partial z}\frac{\partial w}{\partial x} - \frac{1}{2}\frac{\partial u}{\partial x}^2$ in red and $Q_x = -\frac{\partial v}{\partial z}\frac{\partial w}{\partial y} - \frac{1}{2}\frac{\partial v}{\partial y}^2$ in green), then normalize them and only plot positive isosurface values 0.02 for clarity (negative values

give counter-rotating features).

The result is strikingly consistent with instabilities of a transitional mixing layer (Metcalfe et al., 1987; Lesieur, 1990), the transition being constrained by surfzone width. $Q_y$ shows spanwise "rolls" created from the primary instability while $Q_x$ identify streamwise "ribs" that are transverse (counter-rotating) vortices from secondary instability (assumingly growing from perturbations generated between the rolls, in the braid region). Note that streamwise designate the shear direction, which is cross-shore rather than (oblique) wave direction. The reason is that the undertow aligns with surface flow in the alongshore direction, forming only weak mean longshore vertical shear. (Fig. 6). However, the rips can take an oblique direction as they are advected by the mean longshore flow. They extend seaward beyond the surfzone while stretching in the vertical direction. Filaments of vertical vorticity (or $Q_z$, not shown) also have similar rib structures to $Q_x$, recognisable in the surface vorticity plot of Figure 7.

The mean shear flow is composed of breaking-induced mean onshore flow and associated seaward undertow (Fig. 6). The inflected velocity profile is inviscidly unstable to small perturbations and unstable modes of Kelvin-Helmholtz type can emerge. The spanwise rolls are large vertical eddies that rapidly evolve into transverse (streamwise) rib vortices connected by "braid" regions, and stretched seaward and downward. This picture is reminiscent of descriptions based on laboratory-scale measurements and simulations (Nadaoka et al., 1989; Watanabe et al., 2005; Kirby and Derakhti, 2019) — although here no air mixing by bubbles is required for the secondary instability to occur.

According to linear stability analyses, the wavelength of primary shear instability setting the distance between spanwise rolls is an order of magnitude larger than the mixing layer width $\delta$ — in free shear layers (Michalke, 1964, 1965), wavelength, frequency and growth rate of the most unstable modes are 14 $\delta$, 0.015 $U/\delta$ and 0.1 $U/\delta$ respectively). The secondary instability wavelength is of the same order as that of the primary instability (2/3 in Pierrehumbert and Widnall 1982). If the mixing layer width is taken as the vorticity thickness $\delta = \Delta U/[\frac{\partial u}{\partial z}]_{max} \sim 60$ cm, then the wavelength of both roll and rib structures is 5-10 m, consistent with our simulation. Note that given an effective resolution of 5-10 $dx$ for

CROCO (Soufflet et al., 2016), a simulation with 1-m grid resolution can only be considered "eddy-permitting" for 3D instability in the present conditions. As for frequency, the mixing layer size would be associated with modes of 0.01-0.04 Hz (25-100 s period), a range usually reserved to surf beat. The model with 3D instability has energy in this range that is lacking in the deep breaking case (see previous section and Fig. 11), but it has excess energy at lower frequency as well, which may result from upscaling through nonlinear interactions (the same spectrum is produced with monochromatic wave forcing; see also Sec. 4.6).

In order to isolate the mechanism of eddy-mean flow interaction, we analyze a solution forced with monochromatic, shore-normal, long-crested waves (3D_MONO_D0 in Tab. 2). This simulation has constant wave forcing in both space and time when averaging over the wave period (11 s). In this case, the same rib structure is generated (Fig. 14) but without the large-scale alongshore variation seen in the full solution (Fig. 7, right panel). A comparison of this simulation with other test cases will be presented in the next section. Here, we analyse the mechanism and patterns of shear production. Figure 15 shows EKE source terms $-\overline{u_i' u_j'} \frac{\partial \bar{u}_i}{\partial x_j}$, that results from eddy-mean flow interaction, i.e., the energy spent by the mean flow to feed rolls and ribs. The largest term is vertical shear production $-\overline{u'w'} \frac{\partial \bar{u}}{\partial z}$ (Metcalfe et al., 1987), with some lesser contribution from cross-shore convergence $-\overline{u'u'} \frac{\partial \bar{u}}{\partial x}$ (all other 7 combinations are negligible). The main production site is in the breaker zone. A maximum value is located just beneath the inflection point in the mean velocity profile (maximum shear represented in Fig. 15 by a thick blue line), consistent with mixing layer instability. The figure also presents a cross-section of mean 3D eddy kinetic energy ($EKE = \frac{1}{2}(u'^2 + v'^2 + w'^2)$, where $u', v', w'$ are fluctuation velocities to the time-mean flow presented in Fig. 6). EKE and shear production have a very similar spatial pattern, although high EKE values extend from the production center in all directions: surface, bottom, shoreward and seaward. The primary rolls are thus produced in the outer surfzone and advected by the mean and eddy flow towards both the inner surfzone and innershelf. EKE transport is stronger at the surface, so that the streamwise filaments extend farther offshore at the surface than at the bottom (despite some amount of vertical stretching as they leave the terrace).

### *4.5. Short-crested waves and the Peregrine process*

An important question of our study concerns the effect of wave variations (frequency and directional spreading) on flash rip generation in a full 3D model. To address this question, it is useful to simplify the problem and progressively add the multiple conditions of variability. In this section, we analyse shore-normal, short-crested wave simulations with shallow or deep breaking (3D_SC_D0 or 2D_SC_D0). Shore-normal conditions prevents the formation of a longshore current and associated horizontal shear instability. In addition, we look at long-crested wave solutions to isolate the effect of 3D instabilities, i.e., the monochromatic solution (3D_MONO_D0), presented in the previous section, and a similar case with JONSWAP frequency spectrum (3D_LC_D0). This latter comparison will help evaluate the effect of frequency spreading on eddy variability before addressing the effect of directional spreading.

Figure 16 compares vertical vorticity for shore-normal, short-crested wave cases. As for oblique waves, deep-breaking leads to a rich vortical field with large filaments extending far offshore, similarly to Boussinesq models. This is confirmed here with a comparison between FUNWAVE-TVD and pseudo-2D CROCO applied to the same configuration. A difference between Boussinesq and pseudo-2D solutions is the effect of 3D dynamics over the innershelf in the latter case, where surface-intensified offshore eddies and filaments present a more fragmented aspect due to forward energy cascade (Uchiyama et al., 2017; McWilliams et al., 2018). However, the full 3D nonhydrostatic model with shallow breaking (Fig. 16, right panel) shows patterns radically different from both Boussinesq and pseudo-2D solutions with regular shorter-scale rib structures that present a more limited cross-shore extension.

Figure 17 presents EKE cross-sections for all shore-normal wave experiments. A striking element of these figures is the presence of large surface and bottom EKE in the shallow breaking cases. This pattern is not a result of shear production and is absent from the monochromatic case (see previous section and Fig. 15). Therefore, it can only result from wave groups associated with frequency spreading. Through wave height modulation, wave groups produce variability in the breaking-induced surface onshore flow and associated undertow. The variability amounts to about half the integrated mean EKE. However, it is much reduced in the deep-breaking case, consistent with depth-averaged model studies

(de Schipper et al., 2014).

We now turn to the effect of directional spreading. In Figure 17, short-crested waves (produced by directional spreading) extend EKE production over a wider surf zone than long-crested waves, were EKE is confined to the breaker zone. However, the seaward extension is much larger in the pseudo-2D model, confirming the impression made from vorticity inspection. Further confirmation is given by vertical EKE integration (and normalization by mean depth; Fig. 18). It highlights 3 regions of eddy energy: the inner and outer surfzone and innershelf. The top panel presents unfiltered data. In this case, 3D instability and wave group forcing dominates eddy production in the outer surfzone. The most striking observation is that the deep-breaking solution has a much larger cross-shore expansion, stretching shoreward with a maximum in the inner surfzone and also 100 m seaward over the innershelf. The difference of EKE profiles between deep and shallow breaking cases is reminiscent of reported dye mixing overestimation by Boussinesq models (e.g., see profiles of dye concentration in Fig. 10 of Hally-Rosendahl and Feddersen 2016).

Short-crested waves do not seem to affect 3D instability, while, on the contrary, shallow-breaking largely affects eddy production associated with the Peregrine process. This is particularly true for seaward extension. This is even clearer using a low-pass filter on velocity fluctuations, removing a large part of variability from 3D instability and wave group forcing (bottom panel of Fig. 18). What remains is closer to the usual definition of surfzone eddies as Very Low Frequency features. They are much more energetic in the deep breaking case (up to 3 times more than shallow breaking), showing a clearer EKE maximum in the inner surfzone and a large patch over the innershelf. This result is consistent with the findings from previous Boussinesq model studies that filaments forced by short-crested waves originate in the inner surfzone, then spread offshore, forming eddies that grow in scale (Johnson and Pattiaratchi, 2006).

### *4.6. 2D and 3D surfzone turbulent cascade*

If there is energy produced by short-crested waves in the inner surfzone of the shallow breaking case, the question is why does it not produced large filaments, as in the deep break-

ing case. We found an answer in computing the spectrum energy flux. In 2D turbulence, the flux of energy is negative and small fluctuations can grow into larger coherent structures. This process is usually involved to explain the growth of filaments and eddies from variable wave forcing (e.g., Johnson and Pattiaratchi 2006; Feddersen 2014).

To check its validity in a 3D model, we performed a wavenumber spectral flux analysis for pseudo-2D and 3D simulations 2D_SC_D0 and 3D_SC_D0 (Fig. 19). The spectral flux is computed as in Marchesiello et al. (2011) by spectral integration of $v$ advection term. Consistently with 2D turbulence there is a strong inverse cascade of kinetic energy (negative flux) in the pseudo-2D model starting from the scale of injection corresponding to short-crested wave forcing (wavelength of 30-40 m here), and there is no direct cascade towards smaller scales. In the 3D case, the turbulent regime is very different. The negative flux of energy produced by variable wave forcing is present but considerably reduced. In addition, there is a second injection at smaller scales that corresponds to the most unstable mode of 3D instability (wavelength of 7-10 m). This small-scale energy travels both backward and forward across the spectrum and thus widens the range of variability associated with 3D instability. In the 3D long-crested wave case 3D_LC_D0, the same spectral flux is produced at small scales but there is no large-scale inverse cascade due to missing injection by short-crested waves.

This analysis confirms that the growth of filaments and eddies associated with the Peregrine process heavily relies on a 2D inverse cascade, but this cascade nearly collapses when extending to 3D dynamics. In this case, vorticity fluctuations generated by waves with a finite alongshore extent can hardly turn into coherent structures, as they do in the 2D paradigm built on depth-averaged models (Johnson and Pattiaratchi, 2006). The shallow water approximation is therefore too restrictive an assumption for nearshore flows.

### *4.7. Oblique waves and horizontal shear instability*

The precedent experiments with shore-normal waves show that shallow breaking tends to hinder the generation of large 2D eddies by short-crested waves, while sustaining forced and intrinsic 3D surfzone eddy dynamics. We now address the case of oblique waves by increasing

obliquity to $D = 20°$ in order to generate longshore currents with larger horizontal shear. From linear stability analysis of a 2D problem (Bowen and Holman, 1989), the wavelength, frequency and growth rate of the most unstable shear waves are $\lambda_h = 2.5L$ and $f_h = 0.07\frac{V}{L}$, $\sigma_h = 0.15\frac{V}{L}$ where $V$ is the longshore current magnitude and $L$ is the longshore current half-width (outer shear). For a narrow, shoreline-intensified jet typical of Grand Popo at mid-tide (Almar et al., 2014, 2015b), shear can be strong ($\sim 0.05$ s$^{-1}$), implying a minimum shear wave period of 5 min, wavelength of 80 m, and growth time $\sigma_h^{-1} = 3$ min.

Forcing long-crested waves ($\sigma_\theta = 0$) with imposed deep breaking (2D_LC_D20), CROCO recovers results that are typical of wave-averaged shallow-water models (or 3D models with deep breaking as in Marchesiello et al. 2016, or Kumar and Feddersen 2017). Figure 20 (left panel) shows an active horizontal shear instability producing shear waves with wavelength consistent with linear theory. Shear waves propagate with the longshore current as they become nonlinearly unstable, generating filaments and eddies that extend offshore. When both horizontal shear instability and short-crested wave vorticity generation are active (with deep breaking), the solution has even more energy (Fig. 20, center panel). However, with shallow breaking, the horizontal shear instability appears much weaker and is replaced again by rib structures associated with vertical shear instability. Both processes appear reduced by vertical shear.

Inspection of the cross-shore profile of mean longshore currents (Fig. 6) may help to understand how shallow breaking undermines horizontal shear instability. With deep breaking, cross-shore advection is inactive and the longshore current remains trapped over the terrace slope (which is steep in Grand Popo, around 1/10), and his outer shear is strong. With shallow breaking, however, the longshore current is advected by the cross-shore recirculation, stretching its profile across the terrace in a way that minimizes the outer shear. Then, the instability growth rate becomes too weak to overcome friction (from turbulence or bottom drag). This process may explain why, for example, Newberger and Allen (2007) did not found horizontal shear instability in their 3D wave-averaged model solutions as opposed to many previous 2D modeling studies (Allen et al., 1996; Slinn et al., 1998; Uchiyama et al., 2009).

This process is verified in Figure 21, showing cross-sections of time-mean and longshore-mean eddy and mean flow features for the four cases with oblique waves. Horizontal shear instability is best assessed with the eddy-mean flow interaction term $-\overline{u'v'}\frac{\partial \bar{v}}{\partial x}$. In all cases, shear production is clearly correlated with outer and inner slopes of the mean longshore current, with stronger production in the outer shear. Deep-breaking cases show strong shear production and large EKE patches centered over the terrace outer slope, where the current shear is strongest. In the case of horizontal shear instability alone (2D_LC_D20), the magnitude is lower than that of 2D_SC_D20, despite similar shear intensity. This indicates an amplification of shear instability by short crested waves as they drive transient intensification of longshore currents.

When comparing with shore-normal wave simulations of deep breaking cases, offshore EKE seems nearly a linear combination of effects from short-crested waves and horizontal shear instability. Offshore EKE extends further than predicted from shear production due to mean and eddy advection, but short-crested waves clearly provide the most efficient process for innershelf eddy activity.

The shallow-breaking cases (3D_LC_D20 and 3D_SC_D20) also features shear production, but within a narrower zone and in shallower water, better controlled by friction. As a result, EKE is significantly reduced. Short-crested waves (3D_SC_D20) appear to amplify the inner surfzone energy (compared with 3D_LC_D20), but in both cases offshore energy is weak. Over the innershelf, the EKE magnitude can be reduced by a factor 4-5.

## 5. Discussion and conclusion

Flash rips and surfzone eddies are traditionally conceived within a depth-averaged framework that involves intrinsic horizontal shear instabilities or/and direct short-crested wave vorticity generation. They are revisited in this study using a 3D nonhydrostatic wave-resolving model applied to a natural beach with ideal longshore-uniform topography (Grand Popo Beach, Benin). We first presented a quick overview of a new free-surface, compressible approach adapted to wave-resolved nearshore dynamics. Its ability to simulate surface gravity wave propagation and nearshore breaking is validated against laboratory experiment.

Then, the model is applied to Grand Popo Beach nearshore circulation generated by waves with frequency and directional spreading. We assume based on comparison with Boussinesq solutions that the essential difference between 2D and 3D models reduces to the vertical profile of breaking acceleration, i.e., deep or shallow breaking. This allows a direct comparison of 2D and 3D frameworks within the same model equations and model setup.

The generation of transient rips by the 3D model is shown to differ considerably from that produced by depth-averaged models, owing to the vertical structure of currents produced by shallow breaking. Processes of both horizontal shear instability and short-crested wave breaking are restricted in a 3D model by the cross-shore vertical recirculation that prevent a strong inverse cascade. Variable wave forcing (in space and time) tends to increase flow variability in the surfzone (especially at the surface and bottom), but it does not translate into large-scale rips streaming far offshore. Usual 2D mechanisms are replaced by a Kelvin-Helmholtz-type instability, generating rib structures with spanwise and streamwise (alongshore and cross-shore) vorticity of intermediate scale between turbulence and large horizontal eddies — periods of 30 s to a few minutes encroaching on the infragravity wave range and wavelength around 5-10 m. Streamwise filaments extend beyond the surfzone but with lower intensity than usual depth-averaged model rips (offshore mean EKE is reduced by 50 percent). Energy spectra and visual inspections of tracer and sediment concentration shows a much better fit of the 3D model patterns to observational data in Grand Popo Beach. Our results thus question the qualitative and quantitative relevance of depth-averaged models for nearshore dynamics. They may explain in particular some overestimation by these models of surf-shelf exchange (Spydell and Feddersen, 2009; Hally-Rosendahl and Feddersen, 2016) and very low frequency (VLF) variability (Feddersen et al., 2011).

These results are representative of mid-tide conditions of a low tide terrace with moderate wave heights. Interestingly, the rib structures that are described here are comparable to the *mini rips* described for similar conditions by Short et al. (1993): *Under typical mid-tide conditions, with waves breaking across the bar, a low 'friendly' surf zone is produced. Waves are less than 1 m and most water appears to head toward the shore. In fact it is return seaward also, both by reflection of the beach face and via the mini rips, even if no rip*

*channel are present. The rips, however, are usually weak, ephemeral and shallow.*

In order to assess the ubiquity of mini rips in the nearshore zone, future 3D studies should address different nearshore conditions. We assume that the result would be particularly sensitive to the penetration depth of wave breaking. As breaking-induced flow and turbulence are mostly produced above trough level, the breaking vertical length-scale would vary as the root-mean-square wave height $H_{rms}$ (Uchiyama et al., 2010). In our model, it is about half of $H_{rms}$. Therefore, in case of higher waves, higher penetration would reduce vertical shear and increase the contribution of horizontal shear instability and short-crested waves in surfzone eddy generation — as seen in overpublicized photos of large roll-up vortices developing during high wave events. The penetration depth in our simulation is a function of subgrid scale turbulence. Changing from Smagorinsky to k-$\epsilon$ models does not fundamentally change the results, while increasing the Smagorinsky coefficient from 0.1 to 0.5 (which is an unrealistic limit, e.g., Canuto and Cheng 1997; Meyers and Sagaut 2006) reduces the vertical shear and largely damps vertical shear instability — the frictional time $h^2/\nu_t$ is then close to the growth time of about 1 minute. In this case, cross-shore advection is reduced and the wave-averaged longshore flow stays closer to the breaker zone. Horizontal shear instability is thus stronger, but the variability associated with short-crested waves, while increasing in the inner surfzone, remains low on the innershelf. Therefore, even with high turbulence, conventional 2D surf-shelf exchange processes are restrained.

Sensitivity to bottom roughness length $z_0$ is another interesting aspect of our tests. We increased $z_0$ from 0.01 to 1 mm. In this case, the drag coefficient goes from about 0.002 to 0.008. Simulations with deep breaking were very sensitive to these values and the largest roughness would completely shutdown horizontal shear instability due to shorter frictional time (decreased from 5 to 2 min, i.e., shorter than growth time of about 3 min), and damp short-crested wave vortical generation. On the contrary, full 3D solutions with shallow breaking are weakly sensitive to bottom roughness, because of surface intensified currents and shorter growth time of 3D instability. These tests inspire further confidence in our results, while they point to an overemphasized importance given to bottom drag in studies using depth-averaged models (e.g., Allen et al. 1996).

Finally, an important question is what exactly in the 3D model counteracts the generation of surf eddies by short-crested waves. Vertical vorticity generation by the Peregrine process can be written as:

$$\frac{\partial \omega_z}{\partial t} = -\frac{\partial F_{br}}{\partial y_c} \tag{22}$$

where $F_{br}$ is the breaking force, extending to the bottom in a depth-averaged model, and $y_c$ is the along-crest direction. Using a breaking parametrization, Clark et al. (2012) propose a scaling relation for vorticity generation of a single wave as $\frac{H_s^3}{h^{2.5}}$, at a maximum in the outer surfzone. However, flash rip generation originates in the inner surfzone in depth-averaged models (Johnson and Pattiaratchi, 2006) and in our deep breaking simulations. The reason is that adding a transient source of vorticity is not enough to generate a horizontal recirculation (with offshore filament). It needs a coastal boundary and an inverse energy cascade that transform vorticity fluctuations into larger-scale coherent structures, as shown by our spectral flux analysis (Sec. 4.6 and Fig. 19). In a 3D turbulent regime, this cascade is much reduced (due to vortex tilting by the shear flow; McWilliams et al. 2018) and the variability generated in the inner surfzone does not translate into large rips jetting offshore. The inhibition of inverse cascade persist with higher viscosity ($C_s = 0.5$), which however damps 3D instabilities. Therefore, tridimentionality is responsible for both counteracting the generation of large horizontal eddies, and favoring that of intermediate-scale 3D mini rips.

In conclusion, our results suggest that nearshore dynamics and transport processes may be dominated by nonhydrostatic dynamics, not only for surface gravity waves as is known since the 19$^{\text{th}}$ century, but also for vortical motions. This conclusion should hold for moderate waves in other applications but further studies should explore the range of waves and morphological conditions encountered in the global coastal ocean.

## Acknowledgement

This research has received support from a consortium of French research agencies, as part of CROCO's development project (GdR CROCO). It was granted access to the HPC

783 resources of CALMIP supercomputing center under allocation P19069. The fieldwork re-
784 ceived support by the French INSU/EC2CO program (Grand Popo Experiment). We also
785 thank H. Michallet for sharing the GLOBEX data, now freely available at `zenodo.org/`
786 `record/4009405`. Apart from these, all data were acquired by the authors and the CROCO
787 source code is freely available at `www.croco-ocean.org`. Both observational and modeling
788 data are available upon request.

## 789 References

790 van der A, D.A., van der Zanden, J., O'Donoghue, T., Hurther, D., Cáceres, I., McLelland, S.J., Ribberink,
791 J.S., 2017. Large-scale laboratory study of breaking wave hydrodynamics over a fixed bar. Journal of
792 Geophysical Research: Oceans 122, 3287–3310.

793 Akan, C., McWilliams, J.C., Uchiyama, Y., 2020. Topographic and coastline influences on surf eddies. Ocean
794 Modelling 147, 101565.

795 Allen, J.S., Newberger, P.A., Holman, R.A., 1996. Nonlinear shear instabilities of alongshore currents on
796 plane beaches. Journal of Fluid Mechanics 310, 181–213.

797 Almar, R., Almeida, P., Blenkinsopp, C., Catalan, P., 2016. Surf-swash interactions on a low-tide terraced
798 beach. Journal of Coastal Research 75, 348–352.

799 Almar, R., Du Penhoat, Y., Honkonnou, N., Castelle, B., Laibi, R., Anthony, E.J., Sénéchal, N., Degbe, G.,
800 Chuchla, R., Sohou, Z., Dorel, M., Mensah-Senoo, T., Quenum, M., Addo K., A., Ibaceta, R., Kestenare,
801 E., Zodehougan, G., Laryea W., S., Lefebvre, J., 2014. The Grand Popo experiment, Benin. Journal of
802 Coastal Research SI 70, pp. 651–656.

803 Almar, R., Kestenare, E., Reyns, J., Jouanno, J., Anthony, E., Laibi, R., Hemer, M., Du Penhoat, Y.,
804 R., R., 2015a. Response of the bight of benin (gulf of guinea, west africa) coastline to anthropogenic
805 and natural forcing, part1: Wave climate variability and impacts on the longshore sediment transport.
806 Continental Shelf Research 110, 48 – 59.

807 Almar, R., Larnier, S., Castelle, B., Scott, T., Floc'h, F., Detandt, G., 2015b. On the use of the radon
808 transform to estimate longshore currents from video imagery. Coastal Engineering 114, 301–308.

809 Almar, R., Lerma, A.N., Castelle, B., Scott, T., 2018. On the influence of reflection over a rhythmic swash
810 zone on surf zone dynamics. Ocean Dynamics , 1–11.

811 Ardhuin, F., Rascle, N., Belibassakis, K., 2008. Explicit wave-averaged primitive equations using a general-
812 ized lagrangian mean. Ocean Modelling 20, 35.

813 Auclair, F., Bordois, L., Dossmann, Y., Duhaut, T., Paci, A., Ulses, C., Nguyen, C., 2018. A non-hydrostatic
814 non-boussinesq algorithm for free-surface ocean modelling. Ocean Modelling 132.

Barthelemy, E., 2004. Nonlinear shallow water theories for coastal waves. Surveys in Geophysics 25, 315–337.

Blaas, M., Dong, C., Marchesiello, P., McWilliams, J.C., Stolzenbach, K.D., 2007. Sediment-transport modeling on southern californian shelves: A ROMS case study. Continental Shelf Research 27, 832 – 853.

Blayo, E., Debreu, L., 2005. Revisiting open boundary conditions from the point of view of characteristic variables. Ocean Modelling .

Bonneton, P., Bruneau, N., Castelle, B., Marche, F., 2010. Large scale vorticity generation due to dissipating waves in the surf zone. Discrete and Continuous Dynamical Systems - series B 13, 729–738.

Borges, R., Carmona, M., Costa, B., Don, W.S., 2008. An improved weighted essentially non-oscillatory scheme for hyperbolic conservation laws. Journal of Computational Physics 227, 3191 – 3211.

Bowen, A.J., Holman, R.A., 1989. Shear instabilities of the mean longshore current: 1. theory. Journal of Geophysical Research: Oceans 94, 18023–18030.

Canuto, V.M., Cheng, Y., 1997. Determination of the smagorinsky–lilly constant cs. Physics of Fluids 9, 1368–1378.

Castelle, B., du Penhoat, Y., Almar, R., Anthony, E., Lefebvre, J.P., Laibi, R., Chuchla, R., Dorel, M., Senechal, N., 2014. Flash rip dynamics on a high-energy low-tide-terraced beach (grand popo, benin, west africa). Journal of Coastal Research 70, 633–638.

Chen, Q., Kirby, J.T., Dalrymple, R.A., Shi, F., Thornton, E.B., 2003. Boussinesq modeling of longshore currents. Journal of Geophysical Research: Oceans 108.

Christensen, E.D., Deigaard, R., 2001. Large eddy simulation of breaking waves. Coastal Engineering 42, 53 – 86.

Cienfuegos, R., Barthélemy, E., Bonneton, P., 2010. Wave-breaking model for boussinesq-type equations including roller effects in the mass conservation equation. Journal of Waterway, Port, Coastal, and Ocean Engineering 136, 10–26.

Clark, D.B., Elgar, S., Raubenheimer, B., 2012. Vorticity generation by short-crested wave breaking. Geophysical Research Letters 39.

Cox, D.T., Anderson, S.L., 2001. Statistics of intermittent surf zone turbulence and observations of large eddies using piv. Coastal Engineering Journal 43, 121–131.

Debreu, L., Marchesiello, P., Penven, P., Cambon, G., 2012. Two-way nesting in split-explicit ocean models: Algorithms, implementation and validation. Ocean Modelling 49–50, 1 – 21.

Derakhti, M., Kirby, J.T., 2014. Bubble entrainment and liquid–bubble interaction under unsteady breaking waves. Journal of Fluid Mechanics 761, 464–506.

Derakhti, M., Kirby, J.T., Shi, F., Ma, G., 2016. Nhwave: Consistent boundary conditions and turbulence modeling. Ocean Modelling 106, 121 – 130.

Derian, P., Almar, R., 2017. Wavelet-based optical flow estimation of instant surface currents from shore-

based and uav videos. IEEE Transactions on Geoscience and Remote Sensing 55, 5790–5797.

Dodd, N., Iranzo, V., Reniers, A., 2000. Shear instabilities of wave-driven alongshore currents. Reviews of Geophysics 38, 437–463.

Dodd, N., Oltman-Shay, J., Thornton, E.B., 1992. Shear instabilities in the longshore current: A comparison of observation and theory. Journal of Physical Oceanography 22, 62–82.

Elgar, S., Guza, R.T., 1985. Observations of bispectra of shoaling surface gravity waves. Journal of Fluid Mechanics 161, 425–448.

Feddersen, F., 2014. The generation of surfzone eddies in a strong alongshore current. Journal of Physical Oceanography 44, 600–617.

Feddersen, F., Clark, D.B., Guza, R.T., 2011. Modeling surf zone tracer plumes: 2. transport and dispersion. Journal of Geophysical Research: Oceans 116.

Floc'h, F., Mabiala, G., Almar, R., Castelle, B., Hall, N., Du Penhoat, Y., Scott, T., Delacourt, C., 2018. Flash rip statistics from video images. Journal of Coastal Research 81, 100–106.

Grasso, F., Castelle, B., Ruessink, G., 2012. Turbulence dissipation under breaking waves and bores in a natural surf zone. Continental Shelf Research 43, 133–141.

Hally-Rosendahl, K., Feddersen, F., 2016. Modeling surfzone to inner-shelf tracer exchange. Journal of Geophysical Research: Oceans 121, 4007–4025.

Henderson, S., Arnold, J., Özkan Haller, H., Solovitz, S., 2017. Depth dependence of nearshore currents and eddies. Journal of Geophysical Research: Oceans 122.

Hilt, M., Auclair, F., Benshila, R., Bordois, L., Capet, X., Debreu, L., Dumas, F., Jullien, S., Lemarié, F., Marchesiello, P., Nguyen, C., Roblou, L., 2020. Numerical modelling of hydraulic control, solitary waves and primary instabilities in the strait of gibraltar. Ocean Modelling 151, 101642.

Johnson, D., Pattiaratchi, C., 2006. Boussinesq modelling of transient rip currents. Coastal Engineering 53, 419 – 439.

Kazakova, M., Richard, G.L., 2019. A new model of shoaling and breaking waves: one-dimensional solitary wave on a mild sloping beach. Journal of Fluid Mechanics 862, 552–591.

Kirby, J.T., 2016. Boussinesq models and their application to coastal processes across a wide range of scales. Journal of Waterway, Port, Coastal, and Ocean Engineering 142, 03116005.

Kirby, J.T., Derakhti, M., 2019. Short-crested wave breaking. European Journal of Mechanics - B/Fluids 73, 100–111.

Kumar, N., Feddersen, F., 2017. The effect of stokes drift and transient rip currents on the inner shelf. part i: No stratification. Journal of Physical Oceanography 47, 227–241.

Kumar, N., Voulgaris, G., Warner, J.C., Olabarrieta, M., 2012. Implementation of the vortex force formalism in the coupled ocean-atmosphere-wave-sediment transport (coawst) modeling system for inner shelf and

surf zone applications. Ocean Modelling 47, 65 – 95.

Lannes, D., Bonneton, P., 2009. Derivation of asymptotic two-dimensional time-dependent equations for surface water wave propagation. Physics of Fluids 21, 016601.

Larson, M., , Kraus, N., 2002. NMLONG: Numerical model for simulating longshore current; Report 2: Wave-current interaction, roller modeling, and validation of model enhancements. Technical Report. Technical Report ERDC/CHL TR-02- 22, US Army Engineer Research and Development Center, Vicksburg, MS.

Lesieur, M., 1990. Turbulence in Fluids. Fluid Mechanics and its Applications, Springer Netherlands.

Lin, P., Li, C.W., 2002. A $\sigma$-coordinate three-dimensional numerical model for surface wave propagation. International Journal for Numerical Methods in Fluids 38, 1045–1068.

Lin, P., Liu, P.L.F., 1998. A numerical study of breaking waves in the surf zone. Journal of Fluid Mechanics 359, 239–264.

Lippmann, T.C., Thornton, E.B., Stanton, T.P., 2016. The Vertical Structure of Low-Frequency Motions in the Nearshore. Part I: Observations. Journal of Physical Oceanography 46, 3695–3711.

Longo, S., Petti, M., Losada, I.J., 2002. Turbulence in the swash and surf zones: a review. Coastal Engineering 45, 129 – 147. Surface and Swash Zone Mechanics.

Lubin, P., Chanson, H., 2017. Are breaking waves, bores, surges and jumps the same flow? Environmental Fluid Mechanics 17, 47–77.

Ma, G., Shi, F., Kirby, J.T., 2012. Shock-capturing non-hydrostatic model for fully dispersive surface wave processes. Ocean Modelling 43-44, 22 – 35.

MacMahan, J.H., Thornton, E.B., Reniers, A.J., 2006. Rip current review. Coastal Engineering 53, 191 – 208. Coastal Hydrodynamics and Morphodynamics Symposium celebrating the academic closing address of Jurjen A. Battjes.

Marchesiello, P., Almar, R., Benshila, R., Larnier, S., Castelle, B., McWilliams, J.C., 2016. On eddy-mixed longshore currents: Video observation and 3d modeling off grand popo beach, benin. Journal of Coastal Research 75, 408–412.

Marchesiello, P., Benshila, R., Almar, R., Uchiyama, Y., McWilliams, J.C., Shchepetkin, A., 2015. On tridimensional rip current modeling. Ocean Modelling 96, 36 – 48. Waves and coastal, regional and global processes.

Marchesiello, P., Capet, X., Menkes, C., Kennan, S.C., 2011. Submesoscale dynamics in tropical instability waves. Ocean Modelling 39, 31–46.

Marchesiello, P., McWilliams, J.C., Shchepetkin, A., 2001. Open boundary conditions for long-term integration of regional oceanic models. Ocean modelling 3, 1–20.

McWilliams, J.C., Akan, C., Uchiyama, Y., 2018. Robustness of nearshore vortices. Journal of Fluid

Mechanics 850, R2.

McWilliams, J.C., Restrepo, J.M., Lane, E.M., 2004. An asymptotic theory for the interaction of waves and currents in coastal waters. Journal of Fluid Mechanics 511, 135–178.

Menesguen, C., Le Gentil, S., Marchesiello, P., Ducousso, N., 2018. Destabilization of an oceanic meddy-like vortex: energy transfers and significance of numerical settings. Journal Of Physical Oceanography 48, 1151–1168.

Metcalfe, R.W., Orszag, S.A., Brachet, M.E., Menon, S., Riley, J.J., 1987. Secondary instability of a temporally growing mixing layer. Journal of Fluid Mechanics 184, 207–243.

Meyers, J., Sagaut, P., 2006. On the model coefficients for the standard and the variational multi-scale smagorinsky model. Journal of Fluid Mechanics 569, 287–319.

Michalke, A., 1964. On the inviscid instability of the hyperbolictangent velocity profile. Journal of Fluid Mechanics 19, 543–556.

Michalke, A., 1965. On spatially growing disturbances in an inviscid shear layer. Journal of Fluid Mechanics 23, 521–544.

Michallet, H., Ruessink, B.G., Vieira Lima Matias da Rocha, M., De Bakker, A., Van Der A, D.A., Ruju, A., Silva, P.A., Sénéchal, N., Marieu, V., Tissier, M., Almar, R., Abreu, T., Birrien, F., Vignal, L., Barthélemy, E., Mouazé, D., Cienfuegos, R., Wellens, P., 2014. GLOBEX: Wave dynamics on a shallow sloping beach, in: HYDRALAB IV Joint User Meeting, Lisbon, July 2014, Lisbonne, Portugal. pp. 1–12.

Nadaoka, K., Hino, M., Koyano, Y., 1989. Structure of the turbulent flow field under breaking waves in the surf zone. Journal of Fluid Mechanics 204, 359–387.

Newberger, P.A., Allen, J.S., 2007. Forcing a three-dimensional, hydrostatic, primitive-equation model for application in the surf zone: 2. application to duck94. Journal of Geophysical Research: Oceans 112.

Özkan-Haller, H.T., Kirby, J.T., 1999. Nonlinear evolution of shear instabilities of the longshore current: A comparison of observations and computations. Journal of Geophysical Research: Oceans 104, 25953–25984.

Penney, J., Morel, Y., Haynes, P., Auclair, F., Nguyen, C., 2020. Diapycnal mixing of passive tracers by kelvin–helmholtz instabilities. Journal of Fluid Mechanics 900, A26.

Peregrine, D.H., 1998. Surf zone currents. Theor. Comput. Fluid Dyn. 10, 295–309.

Pierrehumbert , R., Widnall, S., 1982. The two- and three-dimensional instabilities of a spatially periodic shear layer. Journal of Fluid Mechanics 114, 59 – 82.

de Schipper, M.A., Reniers, A.J., Ranasinghe, R., Stive, M.J., 2014. The influence of sea state on formation speed of alongshore variability in surf zone sand bars. Coastal Engineering 91, 45 – 59.

Scott, T., Castelle, B., Almar, R., Senechal, N., Floch, F., Detandt, G., 2018. Controls on flash rip current hazard on low-tide terraced tropical beaches in west africa. Journal of Coastal Research 81, 92–99.

951 Shchepetkin, A.F., McWilliams, J.C., 2005. The regional oceanic modeling system (roms): a split-explicit,
952 free-surface, topography-following-coordinate oceanic model. Ocean Modelling 9, 347–404.
953 Shi, F., Kirby, J.T., Harris, J.C., Geiman, J.D., Grilli, S.T., 2012. A high-order adaptive time-stepping tvd
954 solver for boussinesq modeling of breaking waves and coastal inundation. Ocean Modelling 43-44, 36 –
955 51.
956 Short, A.D., Hogan, C.L., Safety, A.B., Program., M., 1993. Beaches of the New South Wales coast : a
957 guide to their nature, characteristics, surf and safety. Australian Beach Safety and Management Program
958 Beaconsfield, N.S.W.
959 Slinn, D.N., Allen, J.S., Newberger, P.A., Holman, R.A., 1998. Nonlinear shear instabilities of alongshore
960 currents over barred beaches. Journal of Geophysical Research 103, 18,357 – 18,379.
961 Soufflet, Y., Marchesiello, P., Lemarié, F., Jouanno, J., Capet, X., Debreu, L., Benshila, R., 2016. On
962 effective resolution in ocean models. Ocean Modelling 98, 36–50.
963 Splinter, K.D., Slinn, D.N., 2003. Three-dimensional modeling of alongshore current dynamics, in: Canadian
964 Coastal Conference, Kingston, Ontario, pp. 1–14.
965 Spydell, M., Feddersen, F., 2009. Lagrangian drifter dispersion in the surf zone: Directionally spread,
966 normally incident waves. Journal of Physical Oceanography 39, 809–830.
967 Svendsen, I.A., Madsen, P.A., 1984. A turbulent bore on a beach. Journal of Fluid Mechanics 148, 73–96.
968 Tissier, M., Bonneton, P., Marche, F., Chazel, F., Lannes, D., 2012. A new approach to handle wave
969 breaking in fully non-linear boussinesq models. Coastal Engineering 67, 54 – 66.
970 Uchiyama, Y., McWilliams, J., Shchepetkin, A., 2010. Wave-current interaction in an oceanic circulation
971 model with a vortex-force formalism: Application to the surf zone. Ocean Modelling 34, 16–35.
972 Uchiyama, Y., McWilliams, J.C., Akan, C., 2017. Three-dimensional transient rip currents: Bathymetric
973 excitation of low-frequency intrinsic variability. Journal of Geophysical Research: Oceans 122, 5826–5849.
974 Uchiyama, Y., McWilliams, J.C., Restrepo, J.M., 2009. Wave-current interaction in nearshore shear insta-
975 bility analyzed with a vortex force formalism. Journal of Geophysical Research: Oceans 114.
976 Warner, J., Sherwood, C., Arango, H., Signell, R., 2005. Performance of four turbulence closure methods
977 implemented using a generic length scale method. Ocean Modelling 8, 81–113.
978 Warner, J.C., Defne, Z., Haas, K., Arango, H.G., 2013. A wetting and drying scheme for ROMS. Computers
979 and Geosciences 58, 54 – 61.
980 Warner, J.C., Sherwood, C.R., Signell, R.P., Harris, C.K., Arango, H.G., 2008. Development of a three-
981 dimensional, regional, coupled wave, current, and sediment-transport model. Computers & Geosciences
982 34, 1284–1306.
983 Watanabe, Y., Saeki, H., 1999. Three-dimensional large eddy simulation of breaking waves. Coastal Engi-
984 neering Journal 41, 281–301.

985 Watanabe, Y., Saeki, H., Hosking, R.J., 2005. Three-dimensional vortex structures under breaking waves.
986 Journal of Fluid Mechanics 545, 291–328.
987 Wei, G., Kirby, J.T., Sinha, A., 1999. Generation of waves in boussinesq models using a source function
988 method. Coastal Engineering 36, 271 – 299.
989 Zijlema, M., Stelling, G., Smit, P., 2011. Swash: An operational public domain code for simulating wave
990 fields and rapidly varied flows in coastal waters. Coastal Engineering 58, 992 – 1012.

Table 1: Model setup of CROCO's Grand Popo Beach configuration

| **Model parameters** | **Values** |
|---|---|
| Grid type | Horizontal: rectangular, regular mesh; vertical: terrain following grid with free surface |
| Domain size ($L_x$, $L_y$) | 240 x 542 m |
| Horizontal resolution (dx/dy)<br>Vertical grid (Nz) | 1 m<br>10 levels (dz=10 cm over the terrace) |
| Time step | dt=0.025 s, $dt_f$=0.001 s, $c_{sound}$=200 m/s (pseudo-acoustic) |
| Bathymetry (h) | longshore-uniform low tide terrace derived from March 2014 survey |
| Tides | mid-tide: 1-m depth over the terrace |
| Wave forcing (u,v,w at offshore boundary) | linear wave solutions reconstructed from JONSWAP spectrum with $H_s = 1.15$ m and $T_p = 11$ s |
| Air-sea forcing (u,v,T,S fluxes) | 0 |
| Sediment model (D50, Ws, $E_0$, $\tau_{cr}$) | $D50 = 100$ $\mu$m; Ws=5 mm/s; $E_0 = 10^{-5}$ kg/m$^2$/s; $\tau_{cr} = 0.01$ N/m$^2$ |
| Breaking/turbulence | WENO5-Z shock-capturing advection scheme<br>Smagorinsky SGS model ($C_S = 0.1$) |
| Bottom roughness ($z_0$) | 0.01-1 mm |

Table 2: List of CROCO simulations for Grand Popo Beach.

| Simulation | Breaking | Wave type | Direction | Test |
|---|---|---|---|---|
| 3D_SC_D10 | shallow | short-crested | 10° | Data vs. 3D instab. vs. Peregrine process |
| 2D_SC_D10 | deep | short-crested | 10° | |
| 3D_SC_D0 | shallow | short-crested | 0° | 3D instab. vs. Peregrine process |
| 2D_SC_D0 | deep | short-crested | 0° | |
| 3D_LC_D0 | shallow | long-crested | 0° | |
| 3D_MONO_D0 | shallow | monochromatic | 0° | |
| 3D_SC_D20 | shallow | short-crested | 20° | 3D instab. vs. 2DH instab. vs. Peregrine process |
| 3D_LC_D20 | shallow | long-crested | 20° | |
| 2D_SC_D20 | deep | short-crested | 20° | |
| 2D_LC_D20 | deep | long-crested | 20° | |
| FUNWAVE-TVD | deep | short-crested | 0° | Test of pseudo-2D CROCO |

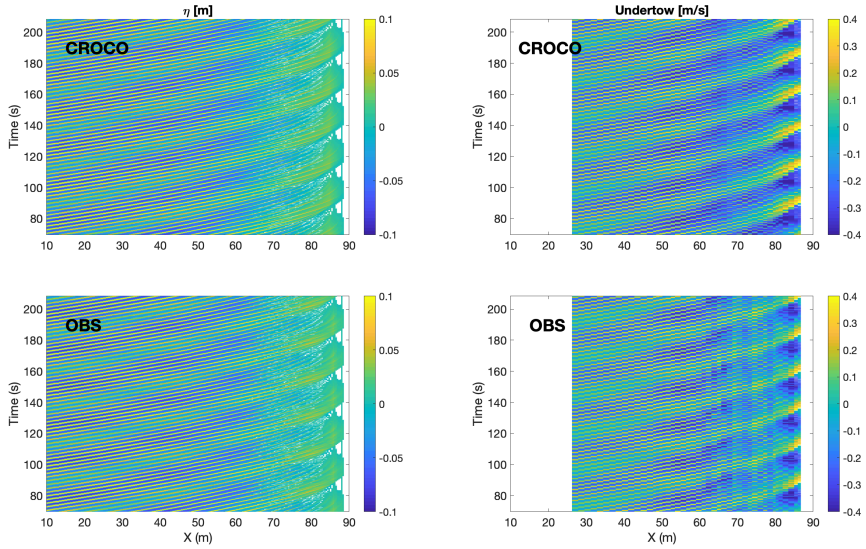


Figure 1: Hovmuller plot (x,time) of data and model sea level $\eta$ and undertow $u_b$ for the GLOBEX B3 flume experiment. When data is missing in the measurements, it is also removed from the model output.

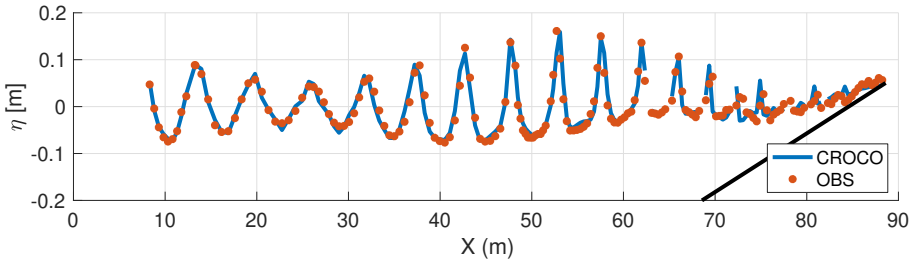


Figure 2: Snapshot of wave field across the GLOBEX B3 flume experiment during runup conditions for model (blue line) and data (red dots).

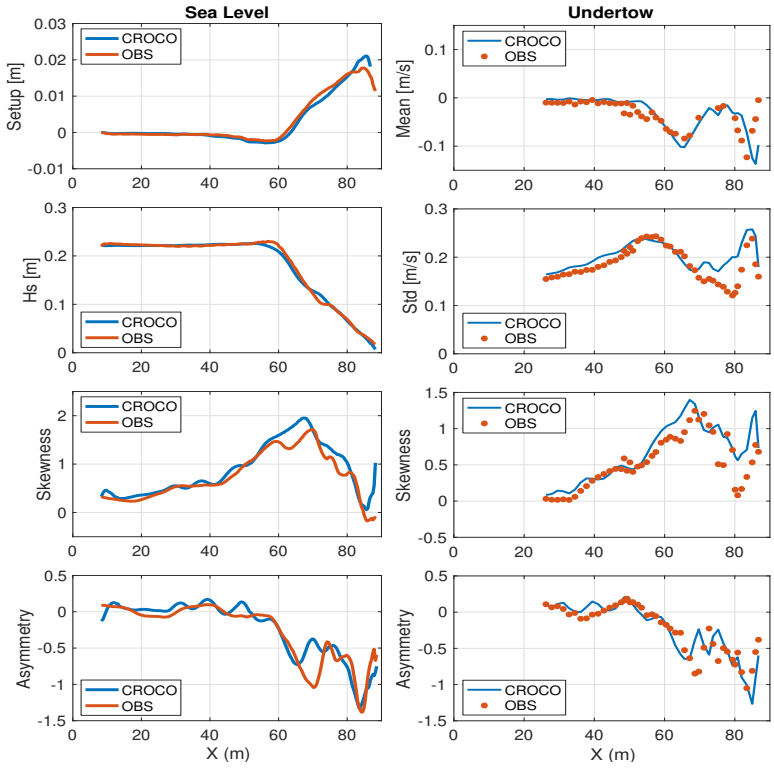


Figure 3: Wave statistics from GLOBEX B3 experiment for sea level $\eta$ (right) and undertow $u_b$ (left) in the model (blue line) and data (red line or dots). From top to bottom: mean, standard deviation (or $H_s$ for $\eta$), skewness and asymmetry.

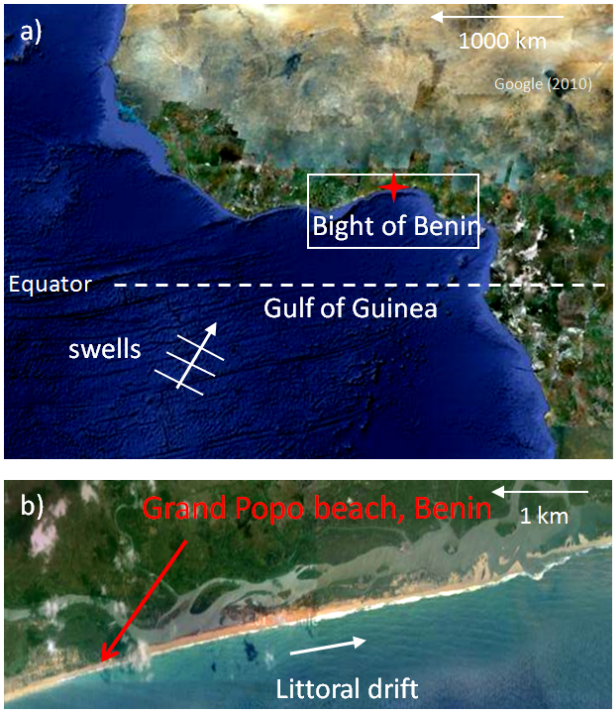


Figure 4: Grand Popo Beach, Benin, is a longshore uniform beach located in the Gulf of Guinea. It is representative of an open, wave-dominated and microtidal environment exposed to S-SW long period swells generated at high latitudes in the South Atlantic.

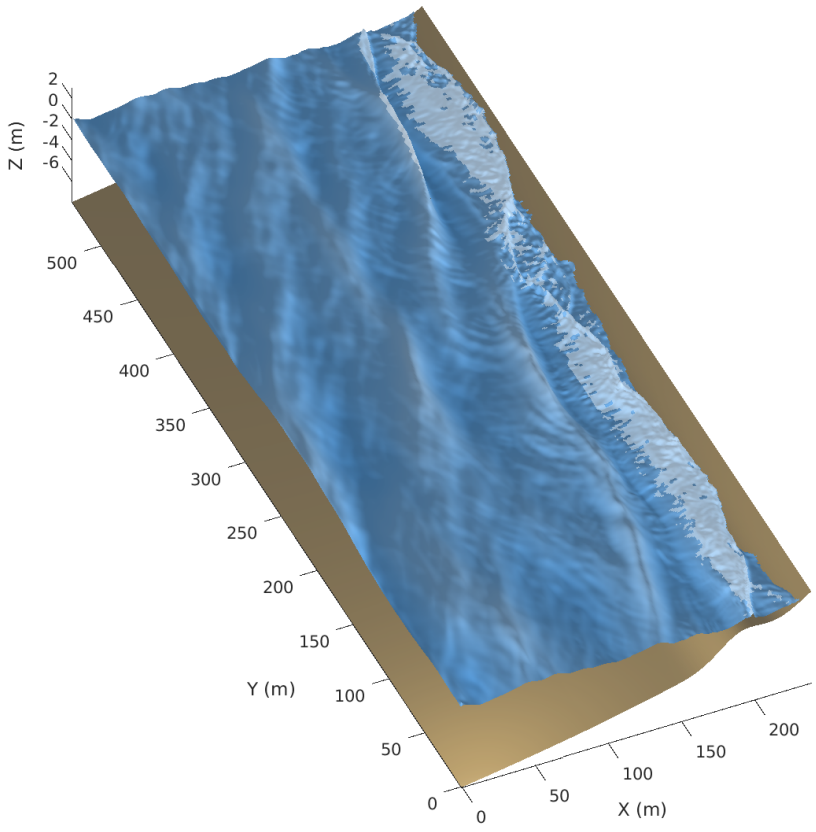


Figure 5: 3D representation of surface waves in CROCO. Short-crested waves are generated at the offshore boundary and propagate shoreward at an angle of 10°, with refraction and breaking through the surf and swash zones. Foam in the surfzone is approximated by white patches in locations of high turbulent kinetic energy of the subgrid-scale model.

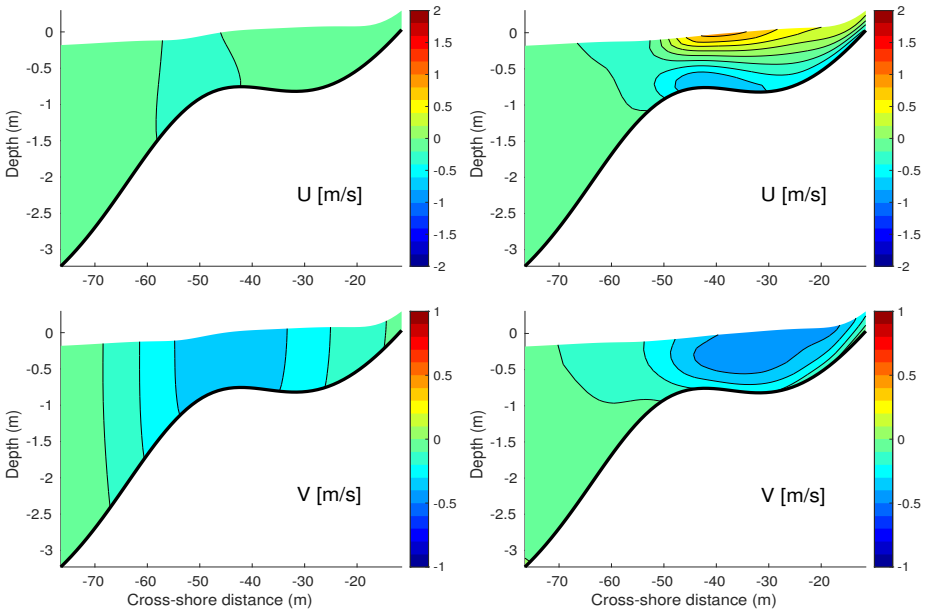


Figure 6: Cross-section of time-mean and longshore-mean, cross-shore (top) and longshore (bottom) currents in the case of shallow (right) and deep (left) breaking.

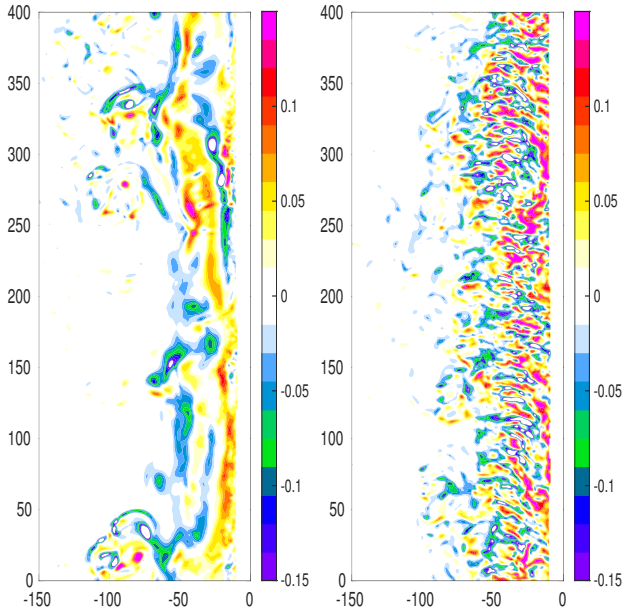

Figure 7: Surface vertical vorticity snapshot in the case of shallow (right) and deep (left) breaking.

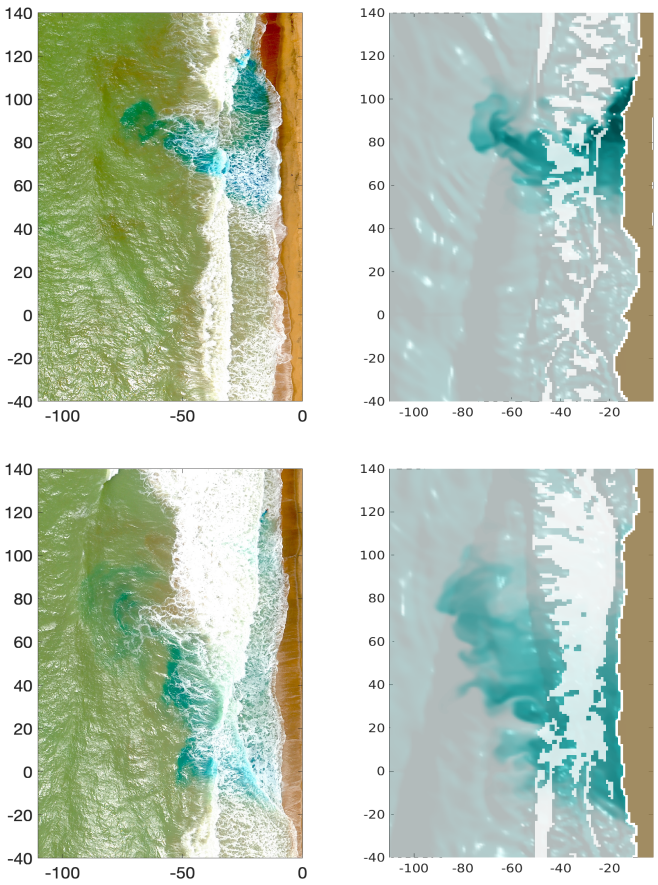


Figure 8: Drone photos (left) and CROCO simulation (right) of dye release at 154 s interval during the Grand Popo survey of March 13 2014 at afternoon mid-tide. In the model, wave surfaces are presented in the background with light from the left (as in the photos), and foam is approximated by high turbulent energy levels as in Fig. 5

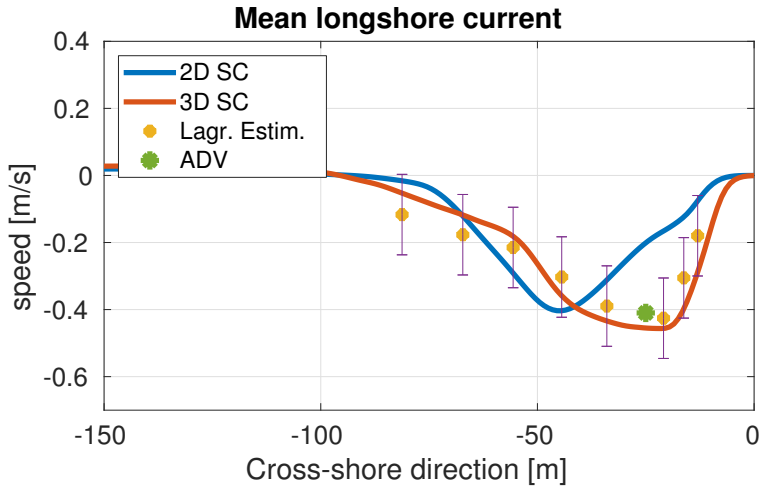


Figure 9: Cross-shore profile of time-mean and longshore-mean surface longshore flow for the full 3D simulation with wave direction $D = 10°$. ADV measurement and an estimation of Lagrangian velocities from drone photos (Fig. 8) is added for comparison.

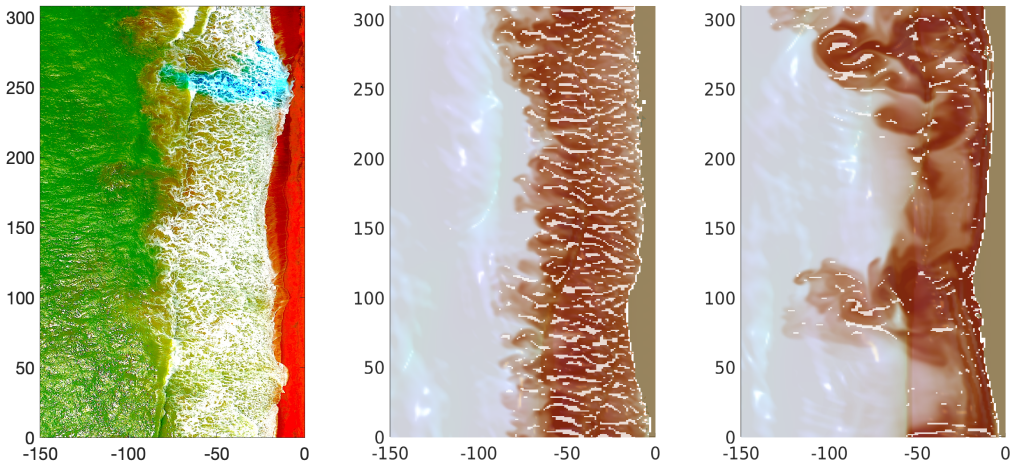


Figure 10: Aerial photo (left) and CROCO simulations of surfzone suspended sediments for shallow-breaking (center) and deep-breaking (right) cases. The contrasts in the photo is enhanced to better expose suspended sediments (brown color). The model suspended sediments correspond to snapshots at 15 min of simulation. Lines of strong alongshore convergence are represented with white patches, to compare with foam structures observed in the photo.

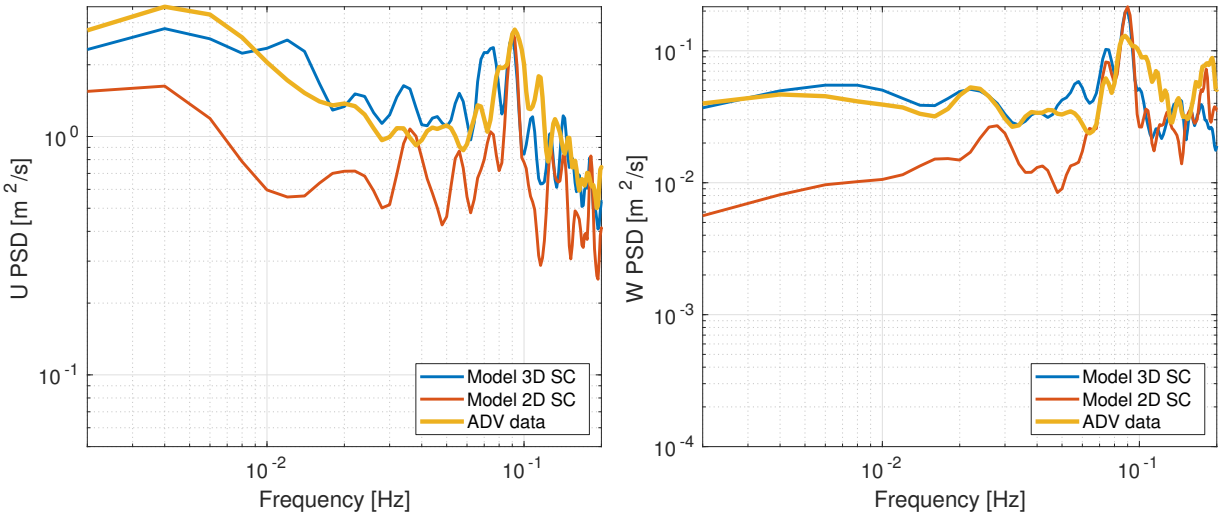


Figure 11: Power Spectral Density of horizontal (left) and vertical (right) velocity fluctuations compared with ADV measurements in the middle of the terrace, in March 13 2014 at afternoon mid-tide.

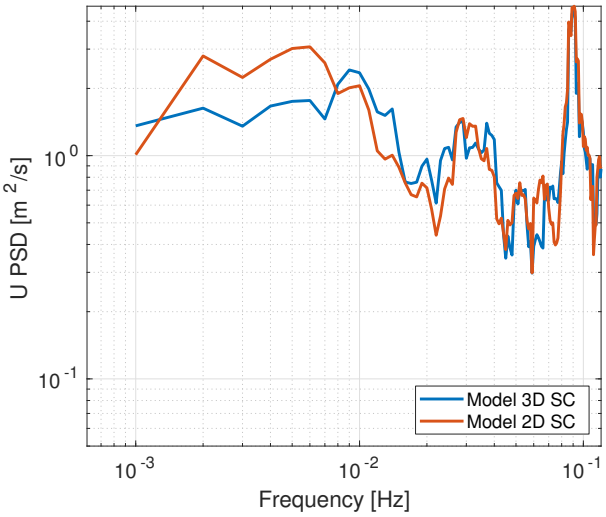


Figure 12: Power Spectral Density of offshore horizontal velocity fluctuations in March 13 2014 at afternoon mid-tide.

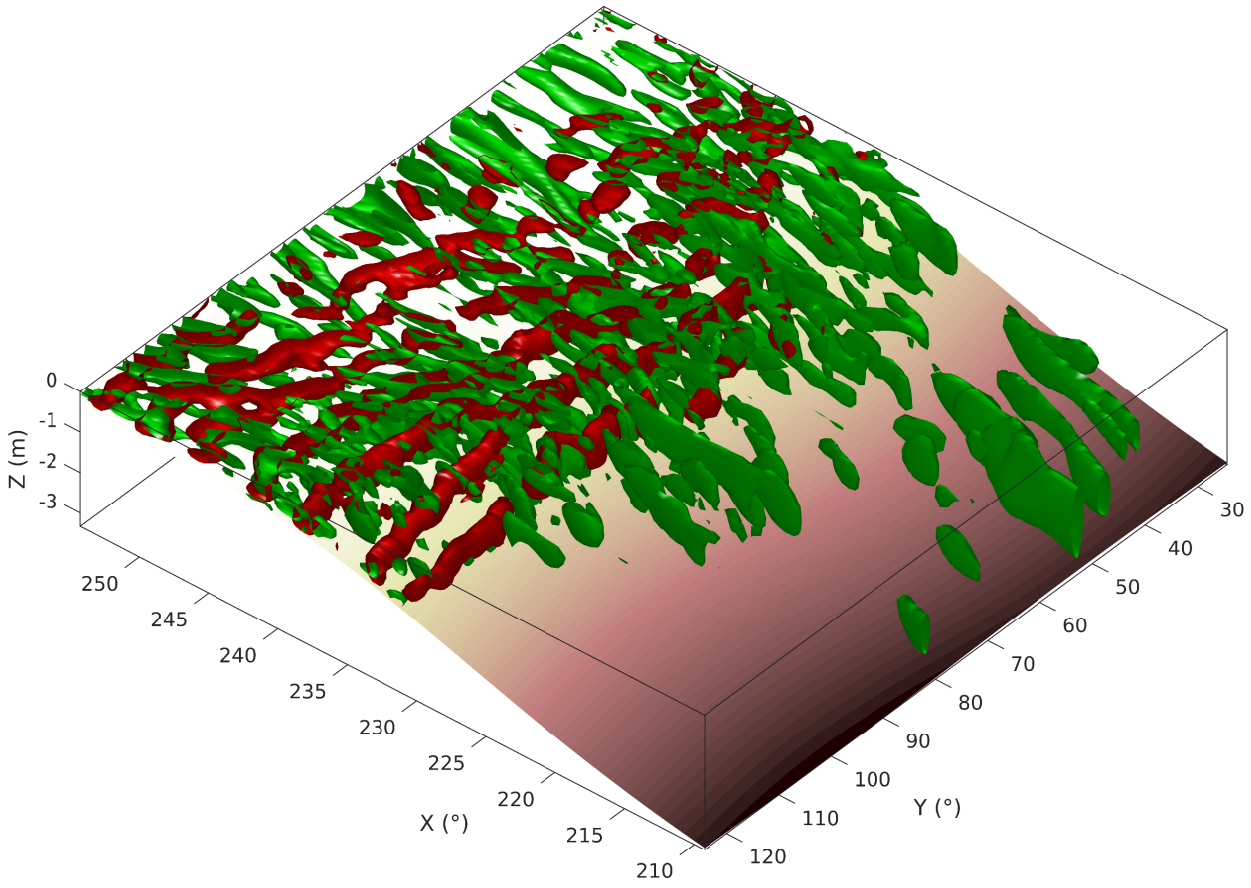


Figure 13: Q field defined by $Q = -\frac{1}{2}\frac{\partial u_i}{\partial x_j}\frac{\partial u_j}{\partial x_i}$, showing coherent structures similar to rolls and ribs in a transitional mixing layer. Cross-shore and alongshore Q terms are split: spanwise rolls (aligned across shear direction) are identified by $Q_y = -\frac{\partial u}{\partial z}\frac{\partial w}{\partial x} - \frac{1}{2}\frac{\partial u}{\partial x}^2$ in red; and streamwise ribs (along shear direction) are identified by $Q_x = -\frac{\partial v}{\partial z}\frac{\partial w}{\partial y} - \frac{1}{2}\frac{\partial v}{\partial y}^2$ in green. The fields are normalized and only positive isosurface values (0.02) are plotted.

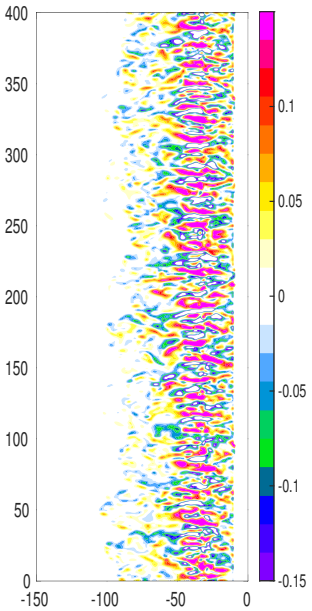


Figure 14: Surface vertical vorticity snapshot for the case with monochromatic shore-normal wave forcing (3D_MONO_D0)

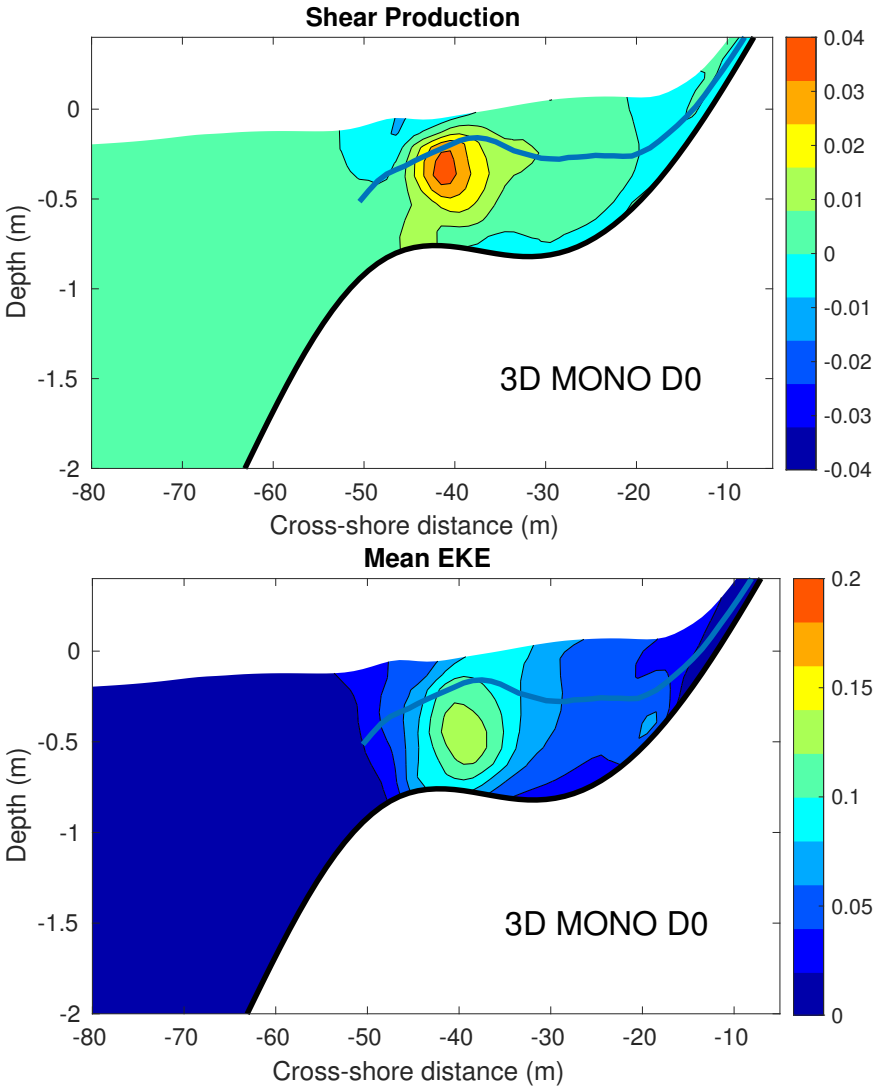


Figure 15: Cross-section of EKE $[m^2/s^3]$ (bottom) and EKE production by the mean shear flow (top) $[m^2/s^3]$ for the case with 3D instabilities only, forced with monochromatic long-crested waves (3DMONOD0). The position of shear flow inflection point is drawn in a blue line

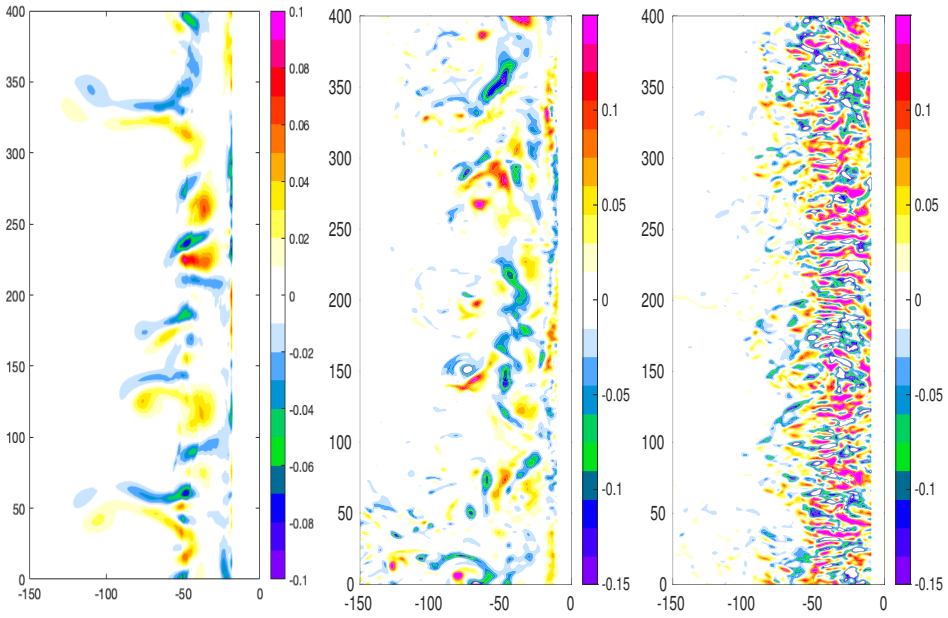


Figure 16: Vertical vorticity snapshot for 3 cases with shore-normal wave forcing: FUNWAVE-TVD (2D Boussinesq) with short-crested waves (left); CROCO with short-crested waves and deep breaking (center); short-crested waves and shallow breaking (right).

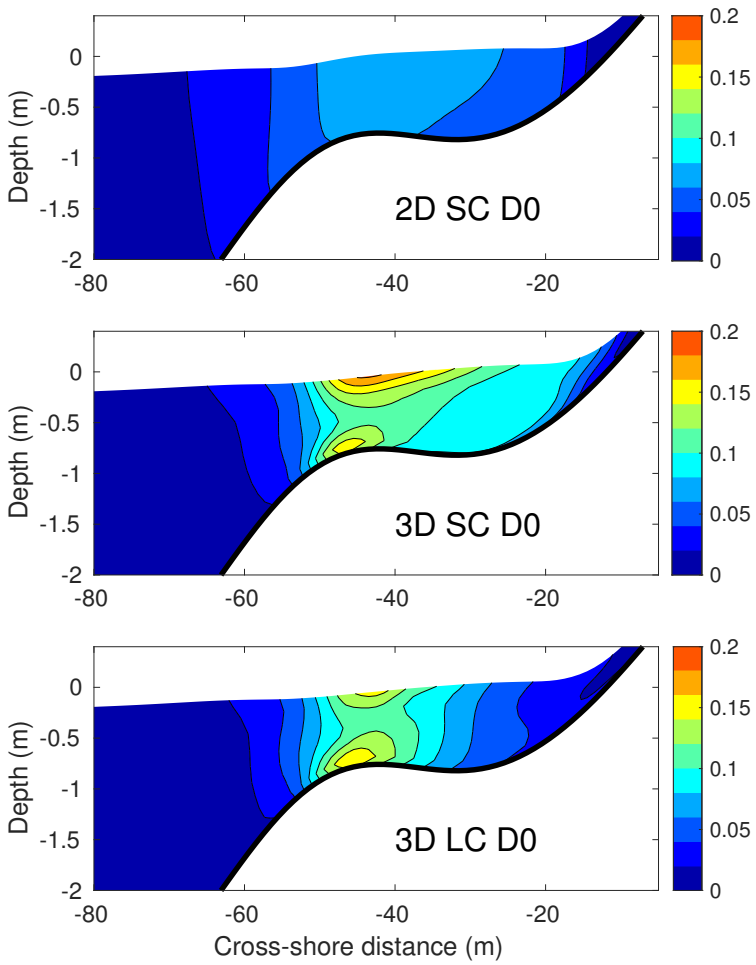


Figure 17: Cross-section of time-mean and longshore-mean EKE for the 3 cases of Figure 16

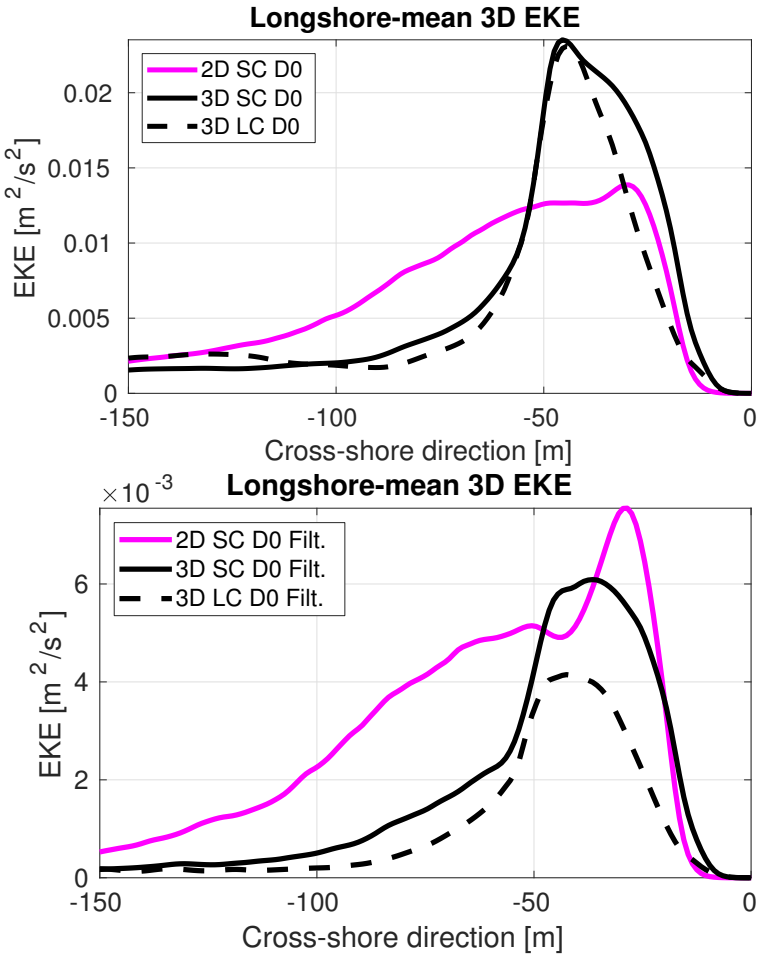


Figure 18: Cross-shore profile of depth-integrated (normalized), time and longshore-mean EKE for the 3 cases in Figure 16. Top: EKE of wave-averaged flow; bottom: EKE of low-pass filtered flow to remove 3D instability modes.

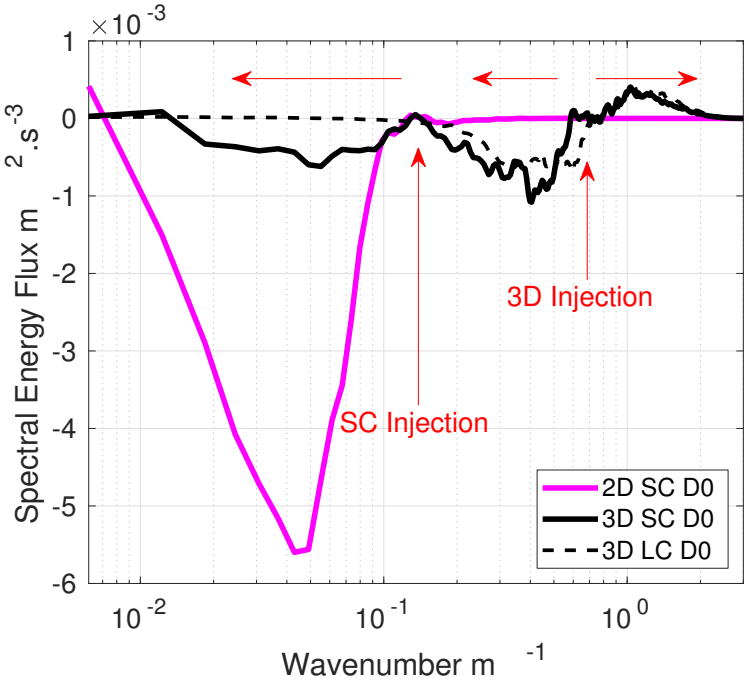


Figure 19: 3D and 2D model wavenumber spectral flux in the surfzone. Vertical red arrows point to the wavenumbers of energy injection from short-crested waves ($\sim$ 40 m wavelength) and from 3D shear instability ($\sim$ 10 m). The spectral flux is computed by spectral integration of $v$ advection term (Marchesiello et al., 2011). Horizontal red arrows indicate positive/negative fluxes, i.e., direct/inverse energy cascade toward smaller/larger scales.

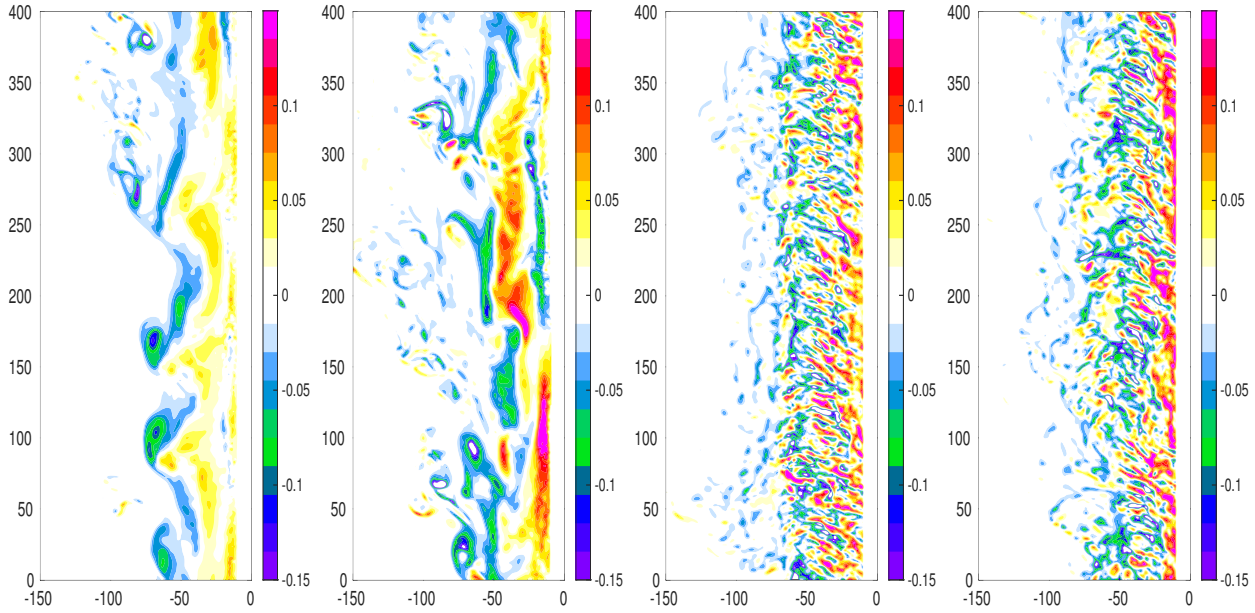


Figure 20: Snapshot of vorticity fields for 4 cases with oblique waves: long-crested waves with deep breaking (2D_LC_D20: first left); short-crested waves with deep breaking (2D_SC_D20: second left); long-crested waves with shallow breaking (3D_LC_D20: first right) and short-crested waves with shallow breaking (3D_SC_D20: last right).

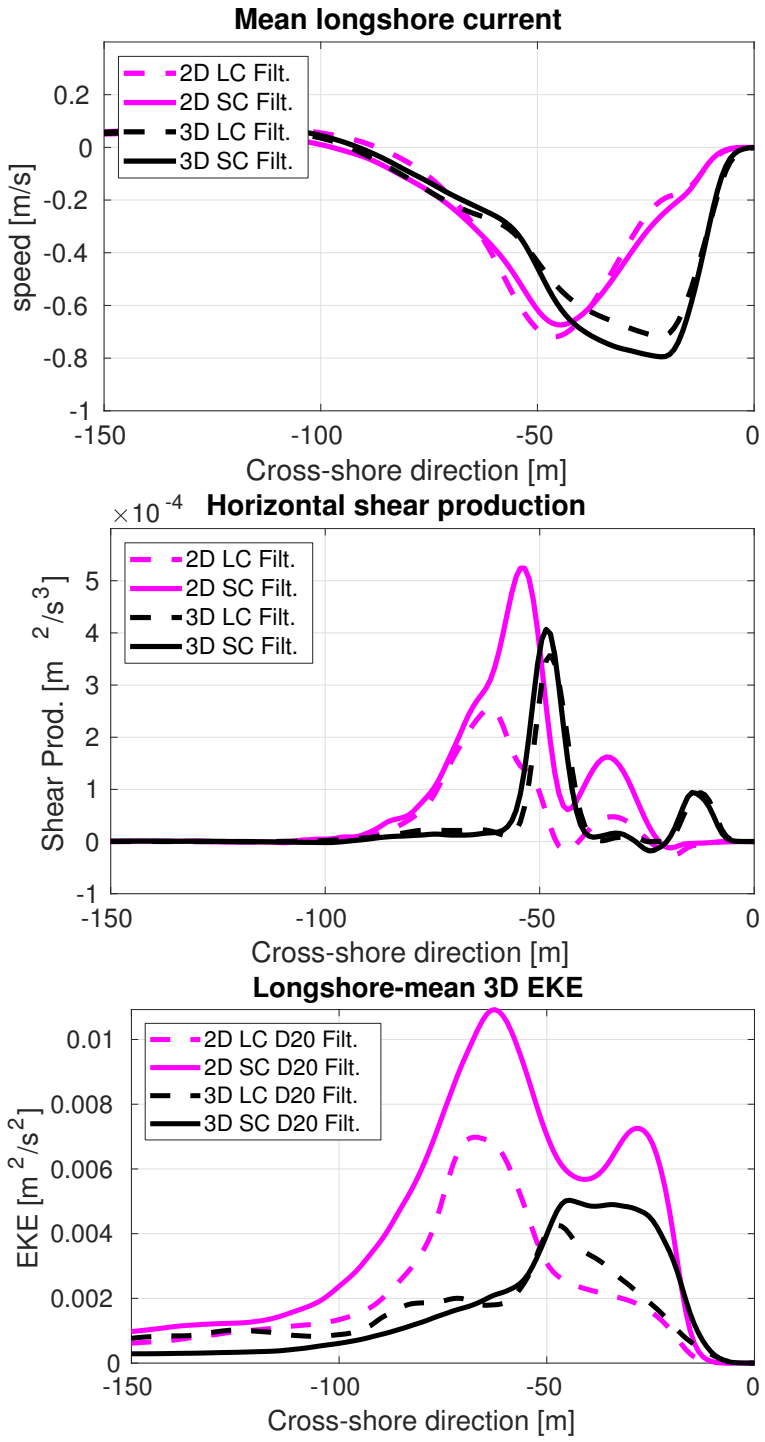


Figure 21: Cross-shore profile of time-mean and longshore-mean flow and eddy statistics for the 4 cases in Figure 16; top: surface longshore flow; center: horizontal shear production $-\overline{u'v'}\frac{\partial \bar{v}}{\partial x}$; bottom: depth-integrated EKE of low-frequency modes.